**The Thesis Committee for Daniel Edgar Bost Certifies that this is the approved version of the following thesis:**

# Growth and Characterization of Amorphous Ultrathin Ruthenium Metal Films

**Committee:**

John G. Ekerdt, Supervisor

Gyeong S. Hwang

# Growth and Characterization of Amorphous Ultrathin Ruthenium Metal Films

**by**

**Daniel Edgar Bost, BS; Ch.E.**

**Thesis**

Presented to the Faculty of the Graduate School of

The University of Texas at Austin

in Partial Fulfillment

of the Requirements

for the Degree of

**Master of Science in Engineering**

**The University of Texas at Austin**

**August 2017**

# Acknowledgements

Many people have helped me over the course of my studies. Prof. John Ekerdt, my adviser, has provided continual advice and knowledge and guided me from the point of first entering the program to the completion of the project. Among the other members of the group who have provided support in the form of knowledge and aid, Lucas Henderson deserves special mention as my unofficial mentor for the first few years, the source of both much of the necessary technical training involved and the previous work that most directly inspires and informs my own. More recently I have worked closely with Wen Liao as a lab-mate, who shared the work of maintaining and designing the experimental apparatus and whom I hope has benefited from my input as much as I benefited from Luke's.

Other members of the Ekerdt research group have provided various levels of advice and aid over the years, as well as the faculty and staff of the Chemical Engineering department and other graduate students too numerous to list in full.

# Growth and Characterization of Amorphous Ultrathin Ruthenium Metal Films

Daniel Edgar Bost, MSE

The University of Texas at Austin, 2017

Supervisor: John G. Ekerdt

Copper interconnect systems in modern microelectronics require the use of one or more liner layers and a capping layer in order to prevent copper diffusion into the other materials of the device. Ruthenium has been suggested as a replacement for the currently-standard Ta/TaN stack used for this purpose due to its low bulk diffusivity of copper and its good adhesion to both substrate materials and copper, but at very low thicknesses the polycrystalline nature of pure Ru allows for diffusion of copper along grain boundaries, resulting in the failure of the barrier. Because amorphous metal alloys do not form grains, amorphous Ru alloys have been examined as a way to eliminate the grain boundary diffusion of copper across the film. Early attempts to produce such films with phosphorus as an alloying element by chemical vapor deposition (CVD) using $Ru_3(CO)_{12}$ and organic phosphorus precursors such as trimethylphosphine have performed well relative to Ta/TaN as a barrier layer at 5 nm thickness. However, high concentrations of carbon were incorporated into the films during CVD by the P precursors. Carbon increases the resistivity of Ru(P) and adds an unnecessary element to the calculated structure of the amorphous alloy.

To reduce resistivity, lower-carbon Ru(P) alloy films are grown at 250 °C using $Ru_3(CO)_{12}$ and a hydride gas ($PH_3$) as the P precursor. Diborane ($B_2H_6$) is used to grow

an alternate alloy, Ru(B). Ru(P) and Ru(B) alloys are predicted by first-principles calculations to be amorphous above 20 at.% P for Ru(P) and 10 at.% B for Ru(B). Growth studies revealed amorphous Ru(P) above 17 at.% P and amorphous Ru(B) above 10 at.% B, with polycrystalline films formed at lower concentrations. Both Ru(P) and Ru(B) are found to deposit as smooth, continuous films at the 3 nm thickness. Metal-insulator-semiconductor (MIS) capacitor structures consisting of copper / amorphous alloy / $SiO_2$ / Si / Al stacks were used to test barrier performance under electrical stress. This testing confirms that the amorphous Ru films perform adequately as Cu diffusion barriers.

# Table of Contents

List of Figures ..... ix

List of Illustrations ..... xi

Chapter 1: Introduction ..... 1

1.1 Background ..... 1

1.1.1 RC Delay and Device Scaling ..... 1

1.1.2 Cu interconnect and Low-*k* Dielectric Materials ..... 3

1.1.3 Selecting Ru as a Copper Diffusion Barrier ..... 5

1.1.4 Amorphous Metals and Amorphous Thin Films ..... 6

1.1.5 First Principles modeling of Ru(P) and Ru(B) amorphous alloys 8

1.1.6 Previous Ru(P) Thin Film Investigation by the Ekerdt Group ... 12

1.2 Objective and Chapter Overviews ..... 13

1.3 References ..... 14

Chapter 2: Experimental Methods and Equipment ..... 18

2.1 Introduction ..... 18

2.2 Method Summaries and Equipment ..... 18

2.2.1 Deposition Method - Chemical Vapor Deposition ..... 18

2.2.2 Deposition Method - Plasma-assisted Physical Vapor Deposition 21

2.2.3 Analysis - X-Ray Photoelectron Spectroscopy (XPS) ..... 22

2.2.4 Analysis - Resistivity Measurements ..... 27

2.2.5 Analysis - X-Ray Reflectivity (XRR) ..... 27

2.2.6 Analysis - X-Ray Diffraction (XRD) ..... 28

2.2.7 Analysis - Atomic Force Microscopy (AFM) ..... 29

2.2.8 Analysis - Time to Failure (TTF) Testing ..... 30

2.3 References ..... 34

Chapter 3: Reducing the Carbon Content of Ru(P) films by using $PH_3$ as the Phosphorus Source ..... 35
3.1 Chapter Summary / Abstract ..... 35
3.2 Growth and Production of Low-Carbon Ru(P) Films ..... 36
3.2.1 Carbon Content ..... 36
3.2.2 Managing P Incorporation and Variation in Composition with Depth ..... 37
3.2.3 Film Structure and Properties ..... 42
3.2.4 Barrier Performance ..... 45
3.3 The Barrier/Liner Application ..... 49
3.4 References ..... 49

Chapter 4: Ruthenium-Boron Alloy thin Films ..... 50
4.1 Chapter Summary / Abstract ..... 50
4.2 Growth and Production of Ru(B) Films ..... 51
4.2.1 Film Growth using $B_2H_6$ as a B source in Ru(B) CVD ..... 51
4.2.2 Carbon content, Resistivity, and Surface Oxidation of B ..... 53
4.2.3 Film roughness and Temperature Stability ..... 57
4.2.4 Barrier Performance and comparison to Amorphous Ru(P) ..... 60
4.3 The Barrier/Liner Application ..... 62
4.4 References ..... 63

Chapter 5: Research Summary ..... 64
5.1 Summary of Results ..... 64
5.1 Conclusions ..... 65
5.2 Recommendations for Future Research ..... 65

References ..... 67

# List of Figures

Figure 1.1: Variation in the mixing enthalpy for amorphous and crystalline Ru(P) and Ru(B) alloys as a function of P(B) content (at.%). The reported values for amorphous alloys are averaged based on three different 64-atom supercells.....10

Figure 1.2: The packing of the solute atoms-centered clusters with an icosahedral ordering of the $Ru_{80}P_{20}$(a), $Ru_{87}B_{13}$(b) and $Ni_{80}B_{20}$(c) alloys. The inner five dark atoms represent P in (a), and B in (b) and (c).....11

Figure 2.1: Deconvolution of the C 1*s* peak.....26

Figure 2.2: Representative XRR spectrum of a thin film.....28

Figure 2.3: A sample of diffraction patterns of crystalline Ru and amorphous films. .....29

Figure 2.4: The current spike associated with capacitive breakdown is observed at 5500 seconds for an Ru(P) film with 25 at.% P under 2 MV/cm electric field stress .....32

Figure 2.5: The three time to failure models, compared to a failure test on an amorphous Ru(P) film at 25 at.% P .....33

Figure 3.1: Analysis of XPS data yields C contents on the order of 10 at.%, unaffected by P content for $PH_3$ films. .....37

Figure 3.2: Rapid P accumulation at the growth surface during deposition results in a dramatic increase in variation of P content vs film depth. The squares are a depth profile obtained from a constant $P(CH_3)_3$ pressure of 1.3 Pa during a 300 C CVD deposition. The circles are a similar, shorter deposition using 1.3 mPa $PH_3$.....38

Figure 3.3: A one-hour Ru(P) growth with the P source removed at 15 min.....40

Figure 3.4: To combat the rapid increase in P accumulation with time, the partial pressure of $PH_3$ is gradually decreased over the course of the deposition cycle. .....41

Figure 3.5: The process outlined in Figure 3.4 results in a relatively unvarying concentration profile, allowing the growth of films that minimize excess surface P while retaining contents above the amorphization target of ~20 at.% P. .....42

Figure 3.6: A sample anneal to crystallization. 3nm film, 25 at.% P. .....44

Figure 3.7: The resistivity of Ru(P) films increases with increased P content....45

Figure 3.8: Pre-averaged data for the low-C Ru(P) film (6 at.% C), giving some idea of the error bars involved in TTF measurements. .....47

Figure 3.9: Time to failure versus field strength for various films; ■ is a 5 nm TaN film grown for comparison purposes, □ is a low-C Ru(P) film (25 at.%P) grown with $PH_3$; ○ is a high-C Ru(P) film (20 at.%P) grown with $P(CH_3)_3$; and, ● is a 5 nm Ru crystalline film with no P. .....48

Figure 4.1: Partial pressure of diborane was decreased in regular steps of 2.5 minutes following an initial higher exposure.....52

Figure 4.2: This composition profile was obtained from XPS analysis of the film grown in Figure 6 there is still some variation in the B content but it was reported as the average (20 at.% B). All films grown had this +/-2 at.% variation. .....53

Figure 4.3: Deconvolution of the C 1s peak for a sample with ~30 at.% P .....54

Figure 4.4: A comparison of the B 1*s* XPS spectra of the oxidized surface of a 15 at.% B Ru(B) alloy film exposed to oxygen in the course of sample transfer (bottom) and the same sample after 20 seconds of Ar+ plasma sputter etching (top), which removes less than 0.1 nm of material from the alloy film.. .....55

Figure 4.5: XRD of a < 10 at.% B Ru(B) alloy film (3-nm thickness), exhibiting strong Ru crystal structure features.....56

Figure 4.6: XRD of a 3-nm 15 at.% B Ru(B) alloy film .....56

Figure 4.7: No correlation between resistivity and B content was observed. .....57

Figure 4.8: Annealing of the 15 at.%B Ru(B) film in section 4.2.3.....59

Figure 4.9: The corresponding anneal to crystallization of a 3-nm film, 25 at.% P (also seen in Chapter 3, reproduced here for ease of comparison) ...59

Figure 4.10: The two tests shown are the 3nm Ru(B) films in section 3.2.4 .....61

Figure 4.11: The 15 at.% B results without the second sample for clarity.....61

Figure 4.12: □ is the median failure time of the 3nm 15 at.% B Ru(B) film. ○ is a 3nm amorphous Ru(P) film reported in Chapter 3. ● is a 5nm Ru crystalline film with no P, grown for comparison in Chapter 3, ■ is a 5nm TaN film grown for comparison in reference [5]. .....61

# List of Illustrations

Illustration 1.1: Interconnect System Cross-section. ..... 2

Illustration 2.1: The geometry of the CVD chamber. ..... 19

Illustration 2.2: The arrangement of various chambers. ..... 22

Illustration 2.3: Schematic layout of an XPS system ..... 24

Illustration 2.4: A barrier testing stack used for TTF analysis ..... 31

# List of Tables

Table 4.1: The first sample was 3.2 nm thick and judged continuous. The second was an attempt to grow a film 2.5-nm in thickness, which was found to be discontinuous.....58

# Chapter 1: Introduction:

## 1.1 BACKGROUND

### 1.1.1 RC delay and Device Scaling

The semiconductor industry has a continuing interest in developing devices with greater device density and speed, roughly in accordance with Moore's Law, coordinating through the International Technology Roadmap for Semiconductors (ITRS) [1] to keep the various specialties within the industry working in parallel. As required component dimensions have decreased, the interconnect (IC) between the transistors has become an increasingly important limiting factor on the speed of integrated circuit electronics. As transistors and other elements are placed more densely within a device, interconnect elements are necessarily also closer to each other, and the role of resistance-capacitance (RC) delay between the interconnect elements themselves becomes a dominant factor in operating speed. Illustration 1.1 shows a sample cross-section of a simple device interconnect, and the 'capacitors' formed by the dielectric material between interconnect elements and the edges of the interconnect itself, all of which can create RC delay, allow crosstalk, and increase power dissipation.

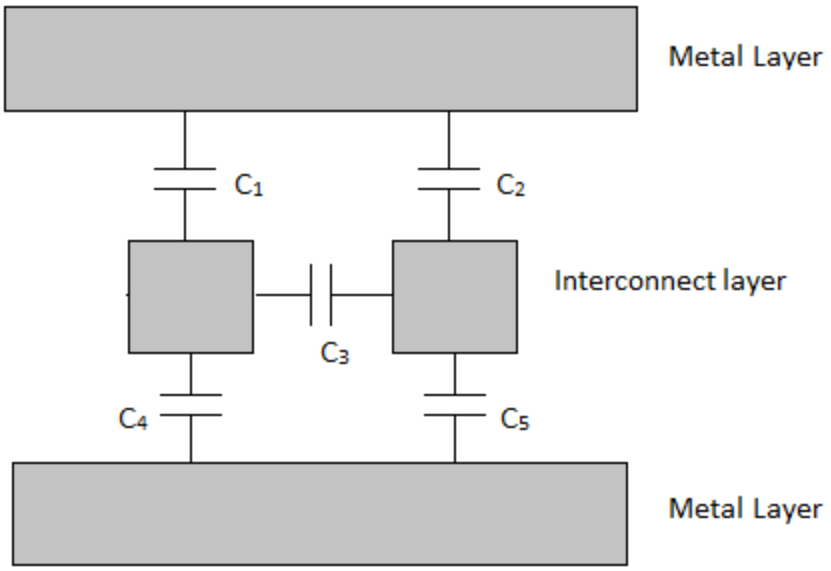


**Illustration 1.1** Interconnect system cross-section.

As linear dimensions decrease, each 'capacitor' formed between the interconnect elements scales with the following formula, where where $A$ is the area of the interconnect elements facing each other, $d$ is the thickness of the material between the two elements and $\varepsilon_r$ and $\varepsilon_0$ are the material's permittivity and the permittivity of free space respectively.

$$C = \varepsilon_r \varepsilon_0 (A/d)$$

Since $A$ is proportional to the square of linear dimensions and $d$ is linearly proportional, the $C$ component of RC increases as overall dimensions decrease. Attempts to mitigate RC delay have taken two major forms: the replacement of $SiO_2$ as the dielectric filler material between interconnect elements with low-$k$ (and thus low permittivity) materials, and the replacement of self-passivating aluminum interconnect with lower-resistivity copper ($\rho_{Cu}$ = 1.7 μΩ·cm and $\rho_{Al}$ = 2.8 μΩ·cm).

### 1.1.2. Copper interconnect and low-k dielectric materials

The introduction of copper to the system has introduced new requirements to interconnect design. While Al's self-passivating nature resulted in the interconnect not interfering with the other materials in the device, copper readily diffuses into both Si [2] and $SiO_2$ [3-5] and forms a variety of copper silicides and oxides, which rapidly results in the degradation and eventual failure of devices. Early low-*k* dielectric materials (such as porous Fluorosilicate Glass or Organosilicate glasses) have also been introduced to further reduce RC delay by reducing the permittivity of the material between interconnect elements. However, these materials can form compounds with Cu near the interface, or trap material in the pores of the material during processing steps, which can oxidize Cu. Additionally, the lower elastic modulus of porous materials can increase the electromigration of Cu through the material [6]. Electromigration is highly dependent on defect densities in the low-*k* materials, especially immediately adjacent to the Cu where damage may be done to the dielectric interface by plasma etching steps during dual-damascene processing [7]. Many of these early problems have been addressed to a limited degree by later advances in the growth of the low-*k* dielectric materials. Techniques have been developed to minimize the processing damage that can lead to greater electromigration of copper in the material [7] or to repair damage with techniques like $CH_4$ plasma exposure [8]. Additionally, curing techniques have been developed to minimize moisture and residual porogen contamination within the pores [8].

While modifications to the dielectric layer or the addition of a modified dielectric liner layer immediately around the interconnect can reduce Cu diffusion into surrounding material, the preferred method has been the addition of a metallic liner layer between the interconnect and dielectric, using a material immiscible with copper. This barrier must

adhere to the dielectric layer for deposition and must also be able to support a copper seed layer for electroplating of Cu during the dual-damascene manufacturing process.

The current diffusion barrier / liner solution is a multi-layer film: TaN, which adheres well to Si and $SiO_2$ and has excellent resistance to Cu diffusion, is deposited on the silicate or low-*k* layer, usually via physical vapor deposition (PVD). A layer of PVD Ta, which has superior adhesion to Cu, is deposited on this, and a layer of Cu is deposited by PVD to act as a seed layer for later copper electroplating [9, 10].

Further decreases in liner thickness requirements have created a strong interest in alternate methods of TaN/Ta deposition and in alternate diffusion barrier materials. As required dimensions shrink below 3 nm, the practical requirements of depositing both layers conformally within the vias and trenches of a Damascene structure, maintaining both film continuity and appropriate film thickness, become more difficult. Reduction of the Cu diffusion barriers to a single film is useful, and removal of the TaN layer to reduce overall thickness is possible, but Ta grown directly on dielectric surfaces has been observed to grow in a higher-resistivity phase (β-Ta $\rho \sim 180\ \mu\Omega\cdot cm$) instead of the lower-resistivity phase observed when grown on TaN (α-Ta $\rho \sim 30\ \mu\Omega\cdot cm$), which can adversely affect electroplating and potentially alter the barrier characteristics of the layer. With barrier thickness requirements approaching 1.9 nm for the 16-nm technology node [11] the exploration of alternate barrier materials compatible with conformal deposition and other manufacturing requirements is vital to meeting device requirements in the near future.

### 1.1.3. Selecting Ru as a Cu Diffusion Barrier

Alternate materials for liners/capping layers have several major requirements to be viable for the application: they should have negligible solubility in copper and vice-versa (indicated by a lack of mixed phases on the relevant binary phase diagram [12] at any temperature potentially involved in processing), they must not form compounds with either Cu or dielectric materials under processing conditions, they should have as low an electrical resistivity as possible, preferably near to or better than that of the Cu interconnect itself, so as not to offset the benefits of Cu, and they must adhere well to both dielectric materials and copper. For obvious cost and scaling reasons, a single-layer solution is desired over replacing the Ta/TaN stack with another multi-layer solution.

Examination of various possibilities fitting these restrictions rapidly drew attention to the refractory metals in general and ruthenium specifically [13]. In addition to having a bulk resistivity of 7 μΩ-cm (less than α-Ta) and a resistivity ~100 μΩ-cm at 3-nm thickness as an amorphous alloy [14, 15] (see also Chapter 3 and 4), Ruthenium is compatible with the direct plating of copper on its surface [16], allowing the removal of an additional step to grow a second alloy film compatible with the Cu seed layer on top of the first Ru layer from the barrier-growth process. Ruthenium can also be grown conformally using chemical vapor deposition (CVD) with well-known precursors such as $Ru_3(CO)_{12}$, with the precursor reacting with the surface of a compatible substrate to leave behind a Ru seed layer, which grows into a film as precursor continues to react with the existing Ru. If the precursor is applied under Knudsen flow conditions, the growth of the film will not be dependent on line of sight to the point of distribution. Many Ru precursors, such as $\eta^4$-2,3-dimethylbutadiene ruthenium tricarbonyl [17] and 1-isopropyl-4-methylbenzene-cyclohexa-1,3-dienyl Ru [18] are also compatible with atomic layer deposition (ALD), where CVD deposition is applied in time-restricted pulses or limited

by a second reaction in cycles to deposit material one monolayer or less at a time, creating films of very uniform thickness and excellent conformality and allowing a high degree of control over film composition and structure. ALD, however, often has the drawback of requiring $O_2$ or $N_2$ as a co-reactant, with the former being especially problematic due to a high tendency to react with other materials in the deposition system in undesired ways.

While unalloyed Ru has been shown to serve as a Cu diffusion barrier in films as low as 15 nm thickness [19], a film of 5 nm or thinner rapidly fails as a diffusion barrier for Cu (see Fig 3.9) due to its vertical columnar grain structure, which at such low thicknesses provides a rapid diffusion pathway for Cu despite its negligible solubility in the interior of the grains [20-22]. This in turn led to interest in the creation of a Ru barrier layer that was lacking in grain boundaries, which would serve as a Cu diffusion barrier consistent with Cu's negligible solubility in Ru due to the lack of alternate pathways for thermal diffusion and electromigration. While amorphous metal-alloy films have been produced using physical deposition methods [23], this work has focused on ALD and CVD methods [21, 24-27]. The material explored in this work involves alloying Ru with P or B to disrupt the crystal structure and cause the films to grow with an amorphous structure, preventing the formation of grain boundaries in the film [21, 28, 29].

### 1.1.4. Amorphous metals and Amorphous thin films

A crystalline solid by definition exhibits a very regular short-range order in the form of the material's crystal lattice, with that order guiding the addition of new metal atoms to the film during film growth, and the lattice oriented according to the disposition

of the atoms in the initial seed. Grain boundaries are the result of two such crystalline domains expanding into each other during film growth but being unable to merge into a single larger crystal due to differing lattice orientations or other mismatch, with the spaces between the grains where they press against each other called the grain boundary. A general review of grain nucleation and growth is included in the chapter references [30].

In the case of ruthenium CVD growth, grains form, grow into each other, and then continue to grow outward from the substrate as further material is added via precursor decomposition. The result is packed columnar grains with the base of each column on the substrate surface, with the boundaries stretching along the entire depth of the film and providing an easy path for Cu migration, which does not require diffusing thorough the grain interiors as noted in the previous section.

Amorphous metals and alloys, by contrast, possess clusters of local order but lack the regularity of an actual crystal lattice [31]. With no lattice mismatches possible due to lack of a lattice, growing grains can simply grow into one another without the creation of borders between distinct grains. However, amorphous alloys such as the Ru(P) and Ru(B) studied in this work are subject to the material re-segregating under annealing to create crystalline grains.

The lack of crystalline regularity, as well as the presence of alloying elements themselves, also alters the transmission of electrons across the material, raising its bulk resistivity above that of the polycrystalline or single-crystalline version of the material. The dimensional restrictions of the thin-film geometry compounds this increased resistivity, with the two factors adding up to the high film resistivities (relative to Ru's bulk resistivity of 7 μΩ-cm) seen in later chapters. Similar susceptibility to annealing

and similar increases in resistivity have been observed in other amorphous thin films such as TaNiSi and TaMoSi [32].

The specific amorphous Ru alloys examined in this work were selected based on computer modeling work done by the Hwang group [33]. *Ab initio* molecular dynamics calculations [33] showed that at approximately 20 at.% P, the presence of the phosphorus should be sufficient to distort the Ru lattice into an amorphous structure exhibiting strong short-range order. Ru-alloy models developed by Hun Woo Kim [34] using first-principles density functional theory were used to analyze these structures and calculate their energetic and chemical bonding properties. Isocahedra were found to dominate medium-range ordering in the amorphous phase, while the atomic size ratio of the alloying element governed short-range ordering [35]. These models were used to compare the total energy of the crystalline phase and the amorphous phase at various composition ratios, resulting in 20 at.% P as the concentration of P necessary in the alloy for the amorphous Ru(P) phase to be energetically stable. A similar model based around disrupting the material's crystallinity with the addition of even smaller boron atoms to the lattice showed that a similar stable amorphous phase occurred at 10 at.% B in a modeled Ru(B) alloy [35].

### 1.1.5. First principles modeling of Ru(P) and Ru(B) amorphous alloys

As mentioned above, predictions were based on first-principles density functional theory (DFT) modeling described more fully in Reference 28, from which the information in this section is drawn. The overall purpose of the modeling was to determine whether amorphous Ru(B) and Ru(P) films could exist in a stable state at room

temperature and to determine the B and P contents necessary to create such stable structures, and to examine the probably microstructure of the metallic glasses.

To examine the relative stability of amorphous versus ordered Ru(P) and Ru(B) alloys, the total energy with varying composition ratios of P and B atoms was calculated particularly in the low content region (below 30 at.% of P and 20 at.% of B), where the transition from a more stable crystalline to amorphous phase was found. The result is summarized in Figure 1.1, which demonstrates that the Ru(P) (Ru(B)) amorphous phase becomes energetically more favorable than its ordered counterpart when the P or B content is above 20 or 10 at.%, respectively. The ordered alloys were calculated by replacing Ru with P or B, starting with the hexagonal close packed structure of pure Ru (with a lattice constant of 2.70 Å). Similarly, the amorphous structures were constructed by replacing Ru with P or B atoms in *a*-Ru; the replacing sites were carefully chosen to ensure homogeneous distribution of P/B. Both ordered and amorphous alloys were modeled using a 72-atom supercell, and the atomic positions and the supercell volume were optimized to minimize the total energy.

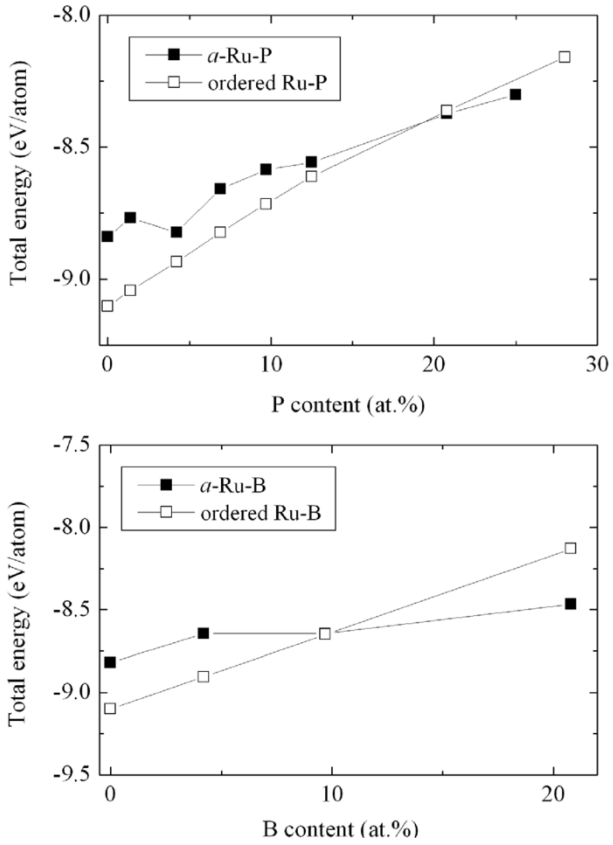


**Figure 1.1** Variation in the mixing enthalpy for amorphous and crystalline Ru(P) and Ru(B) alloys as a function of P(B) content (at.%). The reported values for amorphous alloys are averaged based on three different 64-atom supercells.

The local atomic ordering of Ru(P) and Ru(B) at compositions near the minimums predicted to have stable amorphous phases were then examined using the Voronoi tessellation method [36, 37]. The Ru(P) or Ru(B) alloy with a moderate P or B content resulted in a glassy structure exhibiting a distinct topological and chemical short-range order (SRO). For the *a*-$Ru_{80}P_{20}$ structure (Figure 1.2a), the solute coordination polyhedra form the tri-capped trigonal prism packing arrangement. For *a*-$Ru_{87}B_{13}$

structure (Figure 1.2b), the solute coordination polyhedra form the CN8 Kasper polyhedron.

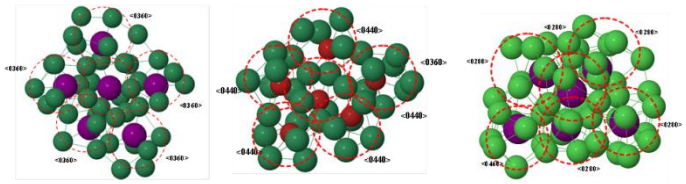


**Figure 1.2** The packing of the solute atoms-centered clusters with an icosahedral ordering of the $Ru_{80}P_{20}$(a), $Ru_{87}B_{13}$(b) and $Ni_{80}B_{20}$(c) alloys. The inner five dark atoms represent P in (a), and B in (b) and (c).

As is shown in Figure 1.2, the formation of 'quasi-equivalent' P-centered Ru clusters arising from topological and chemical SRO is also likely to lead to the medium-range order (MRO) in the binary alloy. In fact, the short-to-medium range order is seen in other metallic glasses, particularly in transition metal-metalloid and transition metal-transition metal systems where the chemical short-range-order is significant [38 - 40]. In $Ni_{80}P_{20}$ [41], the P atom-centered clusters (Figure 1.2c) are packed with the icosahedral order, which is very similar to the topological configuration with the AIMD simulation. In the same manner, Ru(P) has shown the icosahedra type regardless of the type of SRO. These results indicate that the MRO found in the metal-metalloid binary alloy has the icosahedral ordering, which has the most stable packing in metallic glasses.

The primary factor in the change from crystalline to the amorphous phase is the different radii of P and B from Ru, which changes the first-neighbor coordination number of the corresponding lattice element. B's smaller radius compared to P accounts for most of the difference in the concentration necessary to disrupt short-range ordering enough to make the amorphous phase energetically preferable to the corresponding ordered phase.

### 1.1.6. Previous Ru(P) thin film investigation by the Ekerdt Group

A series of publications from Shen, *et al.* [21, 29, 33] documents the initial use of single-precursor CVD (using cis-$RuH_2(PMe_3)_4$) to grow Ru(P) alloy films and then a dual-source CVD method (using $Ru_3(CO)_{12}$ and triphenyl phosphine or trimethylphosphine) to control the P content of the alloy and reliably create Ru(P) diffusion barrier layers of the predicted ideal composition (20 at.% P). These films were found to be amorphous and thus to lack internal grain boundaries as predicted, to deposit conformally on patterned substrates, and to have good adhesion to Cu, Si, and $SiO_2$ as did unalloyed Ru thin films in more recent literature [42]. While promising, these films suffered from high carbon content (and resistivities as high as several thousand μΩ-cm) and could not be grown ultra-thin (<5nm) for practical testing while maintaining continuity.

A later publication by Henderson, *et al.* [43] further explores the dual-source Ru(P) films and their properties. Most directly relevant to the industry's Cu diffusion-barrier application, the paper evaluates the films for performance as diffusion barriers directly by creating Cu / 5 nm Ru(P) / $SiO_2$ / p-Si stacks and testing them to dielectric failure under electrical stress. It was found that 5 nm thick amorphous Ru(P) barriers

performed competitively under this testing against an in-house Ta/TaN barrier film of similar thickness grown for comparison.

## 1.2 OBJECTIVE AND CHAPTER OVERVIEWS

The objective of the work presented here is to better understand the properties of amorphous ruthenium alloy (specifically Ru(P) and Ru(B)) ultrathin films (<5 nm) both during and after growth by chemical deposition methods. Previous work has produced amorphous metal films, but the alloying element precursors have resulted in a large amount of carbon in those films, sometimes as high as 50 at.% C. This work attempts to lower carbon contamination as much as possible to provide a better grounds for comparison with first-principles model calculations and gain insight into the growth process of amorphous metal alloys with CVD, including the migration of alloying elements within the film during growth and the formation of crystalline phases after growth when the films are annealed. The impact of the two alloying elements and of carbon contamination on film resistivity is examined, and Cu diffusion barrier performance under electrical stress is re-evaluated to see if the amorphous films retain their resistance to Cu diffusion and electromigration in the absence of carbon 'stuffing' the structure.

In the interest of examining amorphous films as a diffusion barrier/liner layer in microelectronics (one of the primary source of industry in these materials), the work also attempts to establish that the films can be deposited smoothly and continuously at low thicknesses (3 nm) with CVD and provides a demonstration that they are compatible with the dual-damascene process by producing testing stacks for electrical failure testing.

Chapter 2 provides an overview of the film-growth and analytical methods used in this work, including specific equipment and explanations for various abbreviations used throughout.

The early part of this work builds heavily on the previous work of Lucas B. Henderson with higher-carbon Ru(P) films, and Chapter 3 focuses on the reduction of carbon content by the use of the hydride P precursor phosphine, and re-evaluation of Ru(P) when C is minimally present in the film's composition.

Chapter 4 begins to generalize the properties of amorphous P alloys by examining amorphous Ru(B) and comparing its properties and performance as a barrier to Ru(P).

Chapters 3 and 4 consist primarily of text and figures published in references and [35] and [44].

### 1.3 REFERENCES

[1] P. Gargini, "ITRS Overview", http://www.itrs2.net/itrs-reports.html, July 2015

[2] A. A. Istratov, C. Flink, H. Hieslmair, and E. R. Weber, Phys. Rev. Lett., 81, 1243 (1998).

[3] J. D. McBrayer, R. M. Swanson, and T. W. Sigmon, J. Electrochem. Soc., 133, 1242 (1986).

[4] Y. Shacham-Diamand, A. Dedhia, D. Hoffstetter, and W. G. Oldham, J. Electrochem. Soc., 140, 2427 (1993).

[5] F. Lanckmans and K. Maex, Microelectron. Eng., 60, 125 (2002).

[6] R. Hoofman, G. J. Verheijden, J. Michelon, et al., Microelectronic Engineering 80, 337-344 (2005)

[7] J-Q Zhou, W Sun, H-Y Zhang, et al., ECS Transactions 34(1) 335-341 (2011)

[8] M. Baklanov, J-F de Marneffe, D. Shamiryan, A. M. Urbanowicz, Hualiang Shi, T.V. Rakhimova, H. Huang, P.S. Ho, J. App. Physics 113, 041101 (2013)

[9] K Holloway, P. Fryer, C. Cabral, JME Harper, P. J. Bailey, J. Appl. Phys 71(11) (1992) 5433 -44

[10] L. Y. Yang, D. H. Zhang, C. Y. Li, P. D. Foo, Thin Solid Films 462-463 (2004) 176-181

[11] B-S Nguyen, J-F Lin, D-C Perng, App. Phys. Letters 104 (2014) 082105

[12] T.B. Massalski, "Binary Alloy Phase Diagrams", 2nd ed., pp 1467 (1990)

[13] I. Goswami, R. Laxman, *Semiconductor International 27(5)* pp 49 (2004)

[14] Li et al., Journ. Electrochem. Soc. 154(12) (2007) D642-D647

[15] Fuchs, K.; Mott, N. F., Proc. of the Cambridge Philos. Soc., 34(01) (1938), p.100

[16] Arunagiri, T. N.; Zhang, Y., et al., App. Phys. Lett. 86(8) (2005), pp 083104/1-3

[17] Austin, D.Z., Jenkins, M.A, Allman, D, et al., Chemistry of Materials 29(3) (2017) 1107-1115

[18] Mun, K-Y, Hong, T.E., Cheon, T.; et al., Thin Solid Films 562 (2014) pp 118-125

[19] Lin, JH., Lee, JH., Hsu, CS. et al. Journal of Elec Materi 38: 2251 (2009)

[20] N. Tsyntsaru, G. Kaziukaitis, C. Yang, H. Cesiulis, H. G. G. Philipsen, M. Lelis, J.-P. Celis, J Solid State Electrochem 18 (2014), 3057-3064

[21] J. Shin, A. Waheed, W.A. Winkenwerder, H-W. Kim, K. Agapiou, R.A. Jones, G.S. Hwang, J.G. Ekerdt, Thin Solid Films 515 (2007) 5298-307

[22] L.B. Henderson, J.G. Ekerdt, Thin Solid Films 517 (2009) 1645 - 1649.

[23] D. Cristeaa, b, A. Crisanb, N.P. Barradasc, E. Alvesc, C. Mouraa, F. Vaza, L. Cunha, Applied Surface Science V. 285-A, pp 19-26 (2013)

[24] K. Barmak, C. Cabral, K. P. Rodbell, J. M. E. Harper, J. Vac. Sci. Technol. B 24(6) (2006) 2485-98.

[25] I. Goswami, R. Laxman, Semiconductor Internatl. 27 (2004) 49-54

[26] H. Kim, C. Cabral, C. Lavoie, S.M. Rossnagel J. Vac. Sci. Technol. B 20(4) (2002) 1321-26.

[27] K-Y Mun, T-E Hong, T Cheon, Y Jang, B-Y Lim, S Kim, S-H Kim, Thin Solid Films 562 (2014) 118-125

[28] H. Kim, C. Cabral, C. Lavoie, S.M. Rossnagel J. Vac. Sci. Technol. B 20(4) (2002) 1321-26.

[29] J. Shin, H.-W. Kim, G.S. Hwang, J.G. Ekerdt, Surf. Coat. Technol. 201 (2007) 9256-59.

[30] Venables, J.A; Spiller, GDT; Hanbucken, M; Reports on Progress in Physics 47 (1984) pp 399

[31] Nair, B; Priyadarshini, B.G.; AIMS Materials Science 3 (2016) pp 1022-1053

[32] J.M. McGlonea, K.R. Olsenb, W.F. Sticklec, J.E. Abbottc, R.A. Pugliesec, G.S. Longc, D.A. Keszlerb, J.F. Wagera, Journal of Alloys and Compounds, V 650, pp 102-105 (2015)

[33] J.-H. Shin, A. Waheed, W.A. Winkenwerder. H.-W. Kim, K. Agapiuo, R. A. Jones, G. S. Hwang, J. G. Ekerdt, *Thin Solid Films* 515 (2007) 5298

[34] Hyun Woo Kim, "Structure and properties of amorphous metallic alloys: a first principles study", PhD dissertation, University of Texas Austin, OCLC 700073548 (2010)

[35] D. Bost, H-W Kim, C-Y Chou, G.S. Hwang, J.G. Ekerdt, Thin Solid Films 662 (2017) pp 56 - 64

[36] J. L. Pinney, Proc. R. Soc. A 319 (1970) 479.

[37] J. L. Pinney, Nature 266 (1977) 309.

[38] P. H. Gaskell, Amorphous Metals (eds H. Matyja and P. G. Zielinski), World Scientific Publishing, Singapore, 1985, pp. 35-57.

[39] P. Lamparter, Phys. Scr. T57 (1995) 72-78.

[40] W. K. Luo, H. W. Sheng, F. M. Alamgir, J. M. Bai, J. H. He, E. Ma, Phys. Rev. Lett. 92 (2004) 145502.

[41] H. W. Sheng, W. K. Luo, F. M. Alamgir, J. M. Bai, E. Ma, Nature 439 (2006) 419.

[44] D. Bost, J.G. Ekerdt; Thin Solid Films 558 (2014) pp 160 - 164

[42] Chawla, N., Venkatesh, S.H., Singh, D.R.P. et al. J. of Materi Eng and Perform 22: 1085 (2013)

[43] L. B. Henderson, J. G. Ekerdt, *Thin Solid Films* 517 (2009) 1645

# Chapter 2: Experimental Methods and Equipment

## 2.1 INTRODUCTION

This chapter presents brief overviews of the deposition and analytical methods used in the work presented here, as well as specifics of the equipment employed in the production and analysis of the films.

## 2.2 METHOD SUMMARIES AND EQUIPMENT

### 2.2.1 Deposition Method - Chemical Vapor Deposition

Chemical vapor deposition (CVD) is a method of growing a thin film by placing a substrate into a chamber and flowing one or more precursor chemicals across the substrate's surface where they undergo a chemical reaction to form the film. The rate of growth and the composition of the resulting film is regulated by altering the flow of precursors into the chamber (which changes the partial pressure of each precursor within the chamber and at the growth surface) and altering conditions such as temperature and overall chamber operating pressure.

The CVD system used for this work uses a horizontal sample held on a stage, with a showerhead directly above releasing precursor materials across the substrate surface and a heating bulb below the stage used to control the substrate temperature (Illustration 2.1).

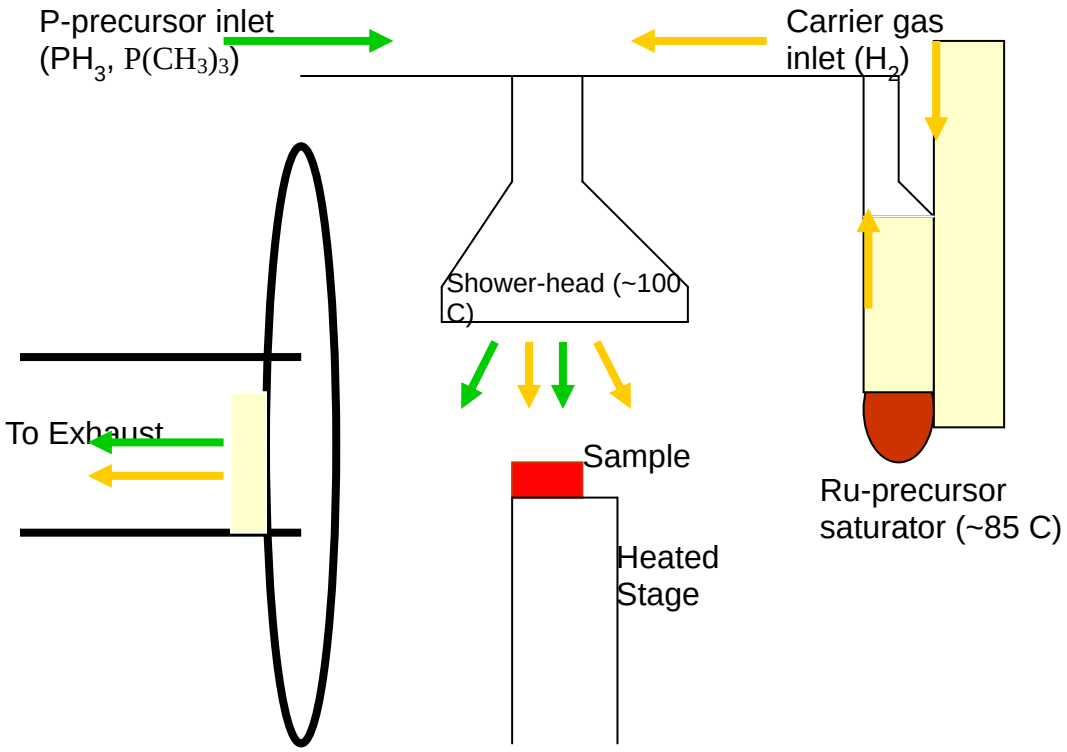


**Illustration 2.1** The geometry of the CVD chamber.

More specifically, films were grown in a cold-wall CVD chamber on 15 kÅ $SiO_2$ deposited using tetraethyl orthosilicate on low-particle undoped Si (Sylib Wafers 812AFBA), with each substrate measuring 20 mm square and anchored to a stainless steel puck used to move it between chambers and position the sample as needed. The Ru precursor, $Ru_3(CO)_{12}$ (Aldrich, 99%), was a volatile solid-state compound distributed from a saturator into the growth chamber using $H_2$ carrier gas, with the saturator kept at 85 °C, the stainless steel tubing before and after the saturator at 90 °C, and the showerhead distributing the gas into the chamber at 100 °C. The Ru precursor and carrier gas was regulated to a flow rate that produced approx. 1.5 Pa partial pressure in the chamber using an electronic mass flow controller (UFC-1500a, Unit instruments). Substrate surface temperature was maintained (at 250 °C where not otherwise specified) by a heating bulb in the stage and controlled with a programmable PID controller running the bulb's power supply, calibrated using a permanent in-situ calibrating puck with a thermocouple. The CVD chamber was kept below 0.7 mPa total pressure between growth cycles.

For Ru(B) film growth, $B_2H_6$ (Voltaix, research grade) at 15 ppm in $H_2$ was flowed into the chamber at flow rates varied to produce $B_2H_6$ partial pressures between 0 and 24 μPa. For Ru(P) film growth $PH_3$ gas (Voltaix, research grade) was introduced to the chamber as a 100 ppm mixture in $H_2$.

Samples grown for electrical testing were instead grown on a p-doped Si substrate with a similar 15 kÅ $SiO_2$ deposited layer.

### 2.2.2 Deposition Method - Plasma-assisted Physical Vapor Deposition (PVD)

PVD is a film deposition method that evaporates or sputters material from a solid target or targets above the substrate sample, causing atoms or molecules from the target to be emitted from its surface and travel across an evacuated space until they hit the substrate and stick, forming a layer that is usually crystalline. The rate of growth of the resulting film can be regulated by altering the plasma power incident on the sputtering target or the temperature of the target for evaporation.

PVD growth is less dependent on the initial 'seeding' of the substrate surface than CVD, and subject to line of sight concerns such as shadowing, whereas CVD is more sensitive to precursors and chemical environment, and conformal. The addition of alloying elements and the regulation of film composition is typically accomplished by altering the relative evaporation or sputtering rate from multiple targets, or by the introduction of a gaseous precursor to the chamber that is incorporated into the film as it grows (regulated by altering the precursor's partial pressure).

The experiments here primarily use PVD for the creation of thicker copper over-layers where precise control of thickness is irrelevant to what is being tested. For example, our setup was amenable to the rapid deposition of crystalline metallic layers, such as ~10 nm Ru for a 30-second deposition at 100 W. Specifically, PVD films were grown using a cold-wall chamber equipped with a rotating stage (hand-turned) and three $Ar^+$ plasma ion sputtering guns (AJA International 320-2a) with interchangeable targets. The Ru target used was 99.999 at.% pure Ru (Kurt J. Lesker & Co), and was sputtered under a 1.3 Pa, 100 W $Ar^+$ plasma (Power controller: Advanced Energy MDX 500), resulting in a Ru deposition rate (on the same 20 mm × 20 mm samples) of 20 nm/min. When not in use, the chamber was held at or below $3\times10^{-5}$ Pa.

The CVD and PVD chambers were connected by a transfer chamber, kept at 1 mPa or lower when not in use, which also connects to the XPS analysis chamber mentioned below and the load-lock to atmosphere. Each individual chamber (including the load-lock) has its vacuum maintained by a separate pump system.

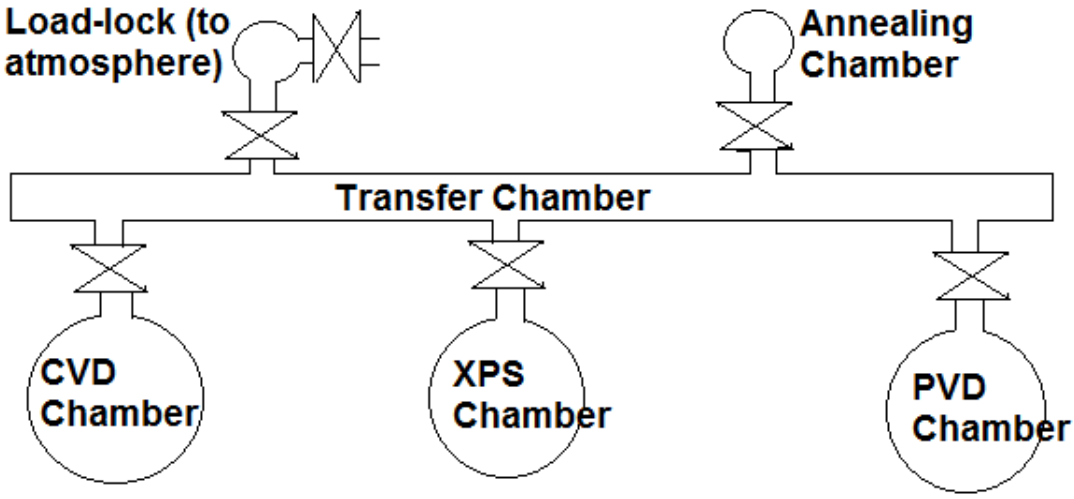


**Illustration 2.2** The arrangement of the various chambers for in situ growth and analysis.

### 2.2.3 Analysis - X-Ray Photoelectron Spectroscopy (XPS)

XPS is a method by which a solid film is subjected to high-energy radiation (specifically X-Rays), while a collector analyzes the kinetic energy of the resulting ejected electrons in order to evaluate their binding energy (Illustration 2.3). The electrons examined are typically core-level electrons not involved in bonding orbitals (such as the Ru $3d_{3/2}$ and $3d_{5/2}$ most frequently examined here), which are excited sufficiently by the X-ray photons to leave the material entirely, making the most

immediate use of this technique the evaluation of a material's atomic composition. A more detailed review of XPS as an analytical technique is included in the references [1].

Because the films being examined are several nanometers thick, the scattering of x-rays within the material can be considered negligible over that length (the Mg Kα x-ray source produces photons with an energy of ~1.3 keV, which has an attenuation coefficient of 2240 $cm^2/g$ [2] and thus an attenuation length of ~27000 $cm^{-1}$) and the only source of signal attenuation is the scattering and re-absorption of ejected electrons traveling through the material. The mean free path of such escaping electrons for varying electron kinetic energies and materials have been extensively tested and tabulated in a NIST database [2] in the form of attenuation lengths (λ) over which an electron has a probability $e^{-1}$ of passing in a given material without being scattered. The strength of an XPS signal emitted at a depth z below the surface is thus:

$$I = I_0 \exp( -z/ (\lambda \cos\theta) )$$

where $I_0$ is the signal strength at the surface of the film (where nothing is above the material to scatter electrons) and $\theta$ is the angle at which the x-ray source and detector are set from normal to the film's surface. The portion of the material that an XPS scan is 'looking at' is thus characterized by the average information depth of $\lambda \cos\theta$, which for the ruthenium thin films is calculated as being between 0.2 and 0.3 nm for the Ru orbitals being examined.

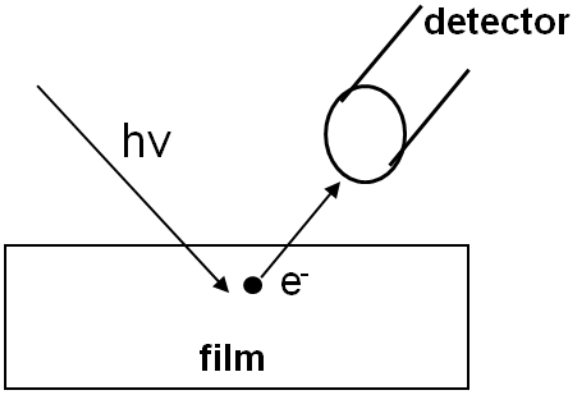


$$E_{\text{binding}} = E_{\text{photon}} - (E_{\text{kinetic}} + \phi)$$

**Illustration 2.3** Schematic layout of an XPS system

The same relationship can also be applied to the substrate layer beneath the film, which in this work is typically Si or $SiO_2$. Taking $I_0$ as the total signal strength of the silicon dioxide substrate, something which can be easily measured in situ with blank samples for calibration, and using the tabulated attenuation length, the actual signal seen from the Si peak is $I$ in the relationship and tells us how thick a layer of Ru the signal has passed through. Since the attenuation length of the Si 1*s* electrons used for this purpose is 0.3 nm in Ru and our Ru alloy films are 3 nm or more thick, some sputtering away of the Ru layer is often necessary to see a Si 1*s* signal. Assuming that the sputter rate is constant and taking the etch rate between two points where the Si 1*s* signal is visible allows us to extrapolate the thickness of the film at previously measured points.

Additional information about the chemical state of the material being examined may also be derived from the specific position of the binding energy peak. Core-level electrons become more tightly bound when the atom is oxidized and less tightly bound to the nucleus when the atom is reduced. This chemical state effect can shift the binding energy up to several eV; however, not all elements display measurable binding energy

shift. These shifts in the position of the peaks are well known, and allow us to check for oxidation of the P (as much as +5.5 eV for the P 2*p* signal in $P_2O_5$) and B (as much as +5.7 eV for the B 1*s* signal in $B_2O_3$) and variations in the chemical state of the Ru atoms (as much as +4.1 eV for the Ru $3d_{5/2}$ signal in $RuO_2$) [2].

The XPS system (Physical Electronics 3057; MgKα, fixed angle at 30°) includes an $Ar^+$ ion sputtering filament, allowing XPS measurements to be taken at regular intervals across the depth of a thin film by sputtering away some material between measurements. Using the attenuation length of the underlying Si 1*s* signal calculated from a NIST database [2], both the thickness of the film and the *in situ* sputter rate were calculated.

Film composition was derived from analysis of the Ru 3*d*, C 1*s*, and P 2*p* XPS peaks. Correcting the peak areas with atomic sensitivity factors tabulated in the literature [3] (4.273 for Ru 3*d*, 0.486 for P 2*p*, and 0.296 for C 1*s*) gives the relative concentration of Ru and P in the films. The C 1*s* peak overlaps the Ru $3d_{3/2}$ peak and has an XPS sensitivity factor an order of magnitude lower, necessitating the derivation of the C 1*s* peak by deconvolution of the Ru 3*d* doublet into two separate peaks, coupled with the known area ratio of the $3d_{5/2}$:$3d_{3/2}$ peaks in a pure Ru sample (1.49:1) (see Figure 2.1). The software [4] uses a Shirley background approximation with three end-points anchored to either side of the doublet, with parameters adjusted until a good fit is achieved for the two peaks. Because of the manual nature of setting the end-points for the background approximation, the process was repeated several times for each sample and the median used for final values. Additionally, it should be noted that this deconvolution technique has an error range of +/-10 at.% (standard deviation calculated by manually setting the baseline for deconvolution five times for each sample) because of the relatively low sensitivity of C in XPS.

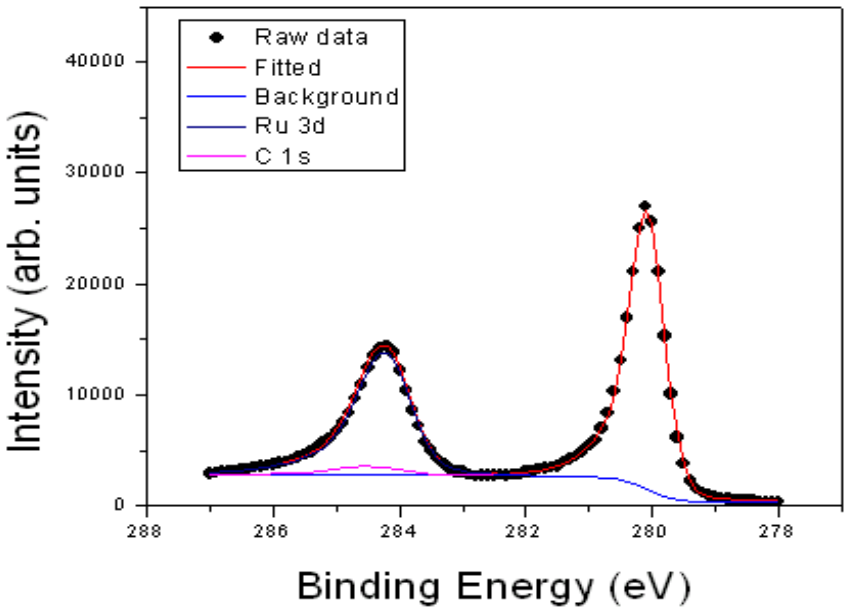


**Figure 2.1** Deconvolution of the C 1*s* peak for a sample with ~30 at.% C

XPS measurements are often used in this work to produce composition depth profiles of films: this is accomplished by alternating composition measurements with Ar+ sputtering steps, with each sputtering step removing a portion of the layer being analyzed from the top down proportional to the length of the sputter. The rate at which the sputter erodes the film (usually a ruthenium alloy film) was determined by the last few composition readings, in which the Si 1*s* peak of the substrate became visible and allowed direct measurement of the thickness of the intervening Ru-alloy layer using the known attenuation length of these emitted electrons in the alloy in question (tabulated by NIST) and the known strength of the Si 1*s* peak for a bare substrate wafer (measured in-situ). Positions of earlier composition measurements where the substrate's signal was not

visible were then determined by applying this derived sputter rate to the specific sputter times. Since each sample's sputter rate was individually re-checked the precise power and character of the sputtering plasma was not kept identical across all samples, though it was never varied for a specific individual sample.

### 2.2.4 Analysis - Resistivity Measurements

Resistivity of films was accomplished by use of an 4-point probe and the x-ray reflectivity (XRR) and XPS-calculated thickness of the film. The film's sheet resistance was measured directly, and the film's resistivity derived from the known relation between resistivity and sheet resistance, where $R_s$ is sheet resistance and $t$ is film thickness:

$$\rho = R_s \cdot t$$

### 2.2.5 Analysis - X-Ray Reflectivity (XRR)

XRR is a method wherein an x-ray beam is applied to a smooth, planar film at a changing angle, with the top and bottom surfaces of the film producing a diffraction pattern as the angle is varied. Source incidence angle was kept constant (0.5 degrees) while the detector angle was varied. The primary use of this method in this work is to determine the thickness of the film being measured. If the film is discontinuous, XRR will not produce a diffraction pattern, and the sample would not be used for further evaluations that assume a continuous film.

The device used for XRR measurements was a Bruker-AXS D8 Advance using a Cu X-Ray source and a scintillation counter detector, and all XRR measurements are ex-situ. A representative spectrum in shown in Figure 2.2.

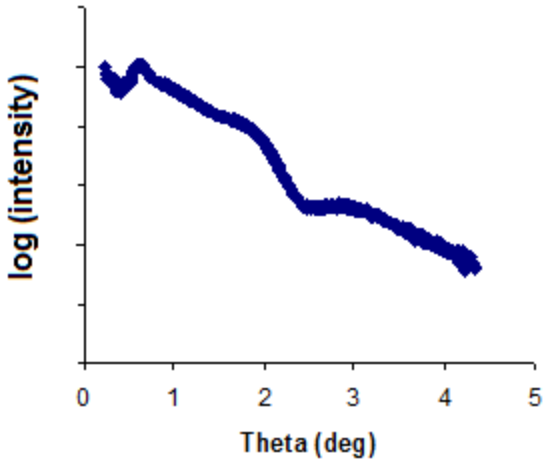


**Figure 2.2** Representative XRR spectrum of a thin film indicating a film thickness of 5.2 nm.

### 2.2.6 Analysis - X-Ray Diffraction (XRD)

XRD is similar to XRR, but instead of the surfaces of the film, the technique uses the spacing of atoms within the crystal lattice to produce a diffraction pattern. This can be used to analyze a variety of aspects of crystal structure, but since this work deals with amorphous films, the technique was used primarily to evaluate whether a given sample was indeed amorphous or whether it was crystalline, both initially and following annealing at elevated temperatures.

Film crystallinity was evaluated through the use of low-angle (0.5 to 1.5 degrees) X-ray diffraction (XRD) (Bruker-AXS D8 Advance with a Cu X-Ray source and a scintillation counter detector, the same physical equipment used for XRR measurements), usually immediately following XRR analysis. Spectra exhibiting no non-Si peaks were judged to be amorphous, and when other crystalline phases appeared they were compared

to known Ru, $Ru_xP_y$ and $Ru_xB_y$ crystalline phases [5] to determine their nature. The low angle of the source serves to maximize the volume of film observed, producing a stronger and more distinctive signal to compensate for the low thickness of the Ru alloy layer. A set of representative spectra are shown in Figure 2.3.

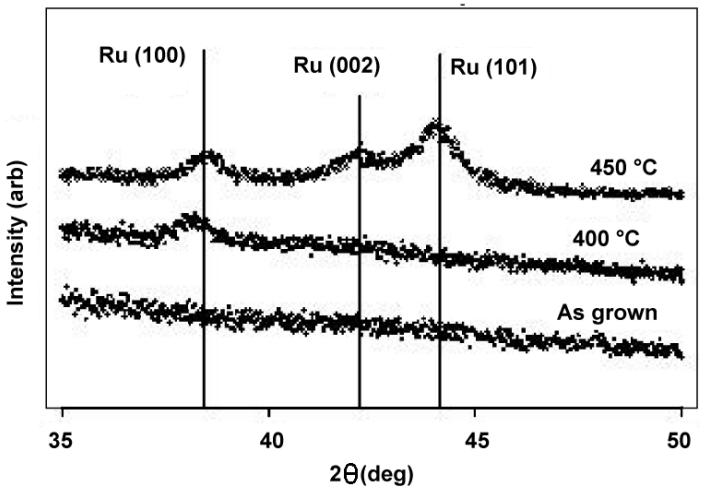


**Figure 2.3** A sample of diffraction patterns of crystalline Ru and amorphous films, which have no pattern or features near possible diffraction peaks.

### 2.2.7 Analysis - Atomic Force Microscopy (AFM)

AFM is a microscopy technique that runs a probe over the surface of a sample to provide a direct measurement of its roughness and the shape of the surface. This probe has the form of a cantilever with a very sharp tip, deflected toward the surface of the sample by attractive forces at close range and away by repulsive forces at even closer range. Deflection in either direction is measured using a laser beam aimed to reflect off the top of the cantilever.

AFM analysis consists of running this probe over the surface of the sample and taking regular measurements of cantilever deflection, with a feedback control loop adjusting the height of the probe in situ to keep it in the range where atomic attractive and repulsive forces result in measurable deflection and creating a map of the surface which can then be analyzed directly to derive factors such as RMS roughness. The AFM used in this work was an Aligent Instruments 5500.

### 2.2.8 Analysis - Time-to-Failure (TTF) testing

TTF testing is a method where a device stack is grown which includes a barrier layer and is analogous to a real device (typically a barrier layer between a layer of copper and a dielectric on doped silicon), and an electrical voltage is applied across the stack until it suffers capacitive breakdown and fails, resulting in a large jump in the measured current.

In our more specific case, a Cu/Ru(P)/$SiO_2$/p-Si stack backed by Al for contact (see Illustration 2.4) was manufactured using the Ru(P) film in question in the following manner: a thick (>10 μm) Cu film was deposited by PVD on top of an Ru(P) film judged to be continuous and amorphous. Examination of Ru(B) alloy films employed a stack with an Ru(B) layer in place of the Ru(P) layer that was otherwise identical in manufacture and composition. A negative-mask photoresist (Microchem ma-N 2403, removable by sonication in acetone) was used to etch 1 mm circles of Cu with a 7% nitric acid bath (removing Cu) and then etched for 10 min under a 20% $O_2$ Ar plasma to remove the Ru(P). The resulting 1 mm "dot" stacks of Cu/Ru(P) separated by bare $SiO_2$ were then patterned with 0.3 mm circles and etched again in $HNO_3$, leaving 0.3 mm diameter dots of Cu atop 1 mm dots of Ru(P) to prevent Cu diffusion around the edges of

the stack. A thick (>10 μm) layer of PVD Al was then deposited on the back-side of the wafer square following abrasion of the surface to provide a conductive, self-passivating backing layer. The masks used for lithography featured many "dots" at regular 3 mm intervals, meaning that a single 20 mm × 20 mm sample could have as many as 36 device stacks for testing. In practice, about half of these tended to be visibly damaged or fail immediately (indicating damage to the barrier/liner layer), limiting the number of samples of a given film to 10 – 15. In a single test, a device stack was placed under a strong field, and the leakage current monitored (Agilent 4156C Semiconductor Parameter Analyzer) for a sudden abrupt increase indicating capacitive failure most likely due to Cu diffusion as seen in Figure 2.4.

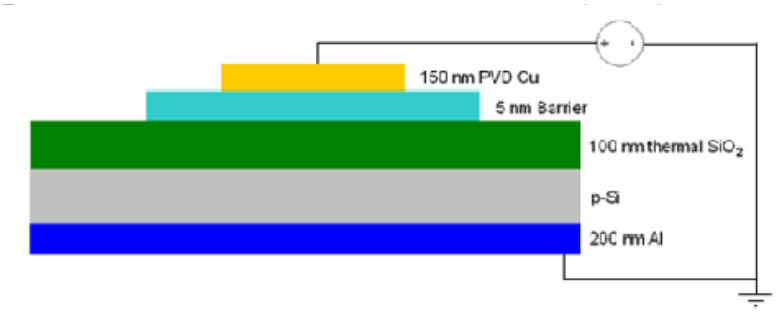


**Illustration 2.4** A barrier testing stack used for TTF analysis

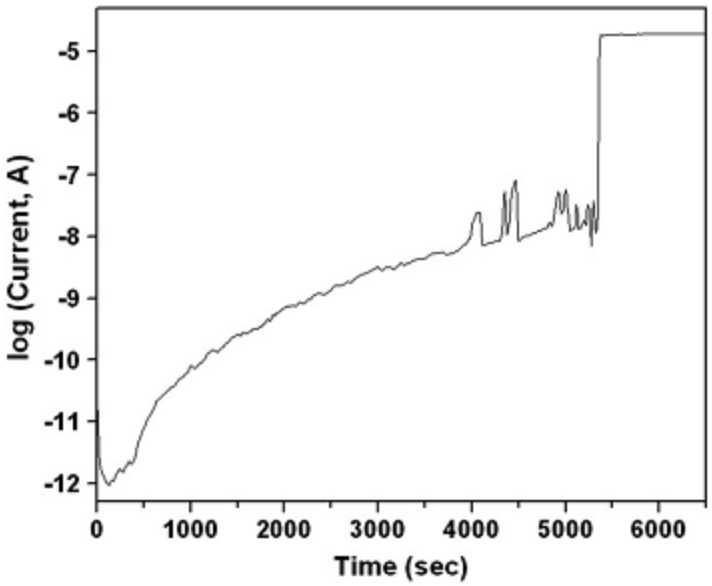


**Figure 2.4** The current spike associated with capacitive breakdown is observed at 5500 sec for an Ru(P) film with 25 at.% P under 2 MV/cm electric field stress

There are three models for the Cu-diffusion driven failure of these capacitor stacks: the E model, which states that the failure time is proportional to the exponential of the electric field, and physically based on the bond breakage within the dielectric, and the 1/E model, which posits that the primary mechanism is Fowler-Nordheim current conduction and thus failure time is proportional to the exponential of the inverse of the electric field. A third model posits that failure is dominated by diffusion of Cu into the dielectric, and proposes $\sqrt{E}$ as the contribution of the field to this failure mechanism [6].

As this work is an examination of barrier properties of various films, projected operational lifetimes are obtained by using the $\sqrt{E}$ model, projected to a typical operating field condition of 0.2 MV/cm for purposes of direct comparison between examined barrier films. Actual direct measurements of operating lifetimes are restricted to field strengths in excess of 2 MV/cm due to time restrictions on the use of equipment. The

differences in the projections of the three models on the same set of experimental data is shown in Figure 2.5.

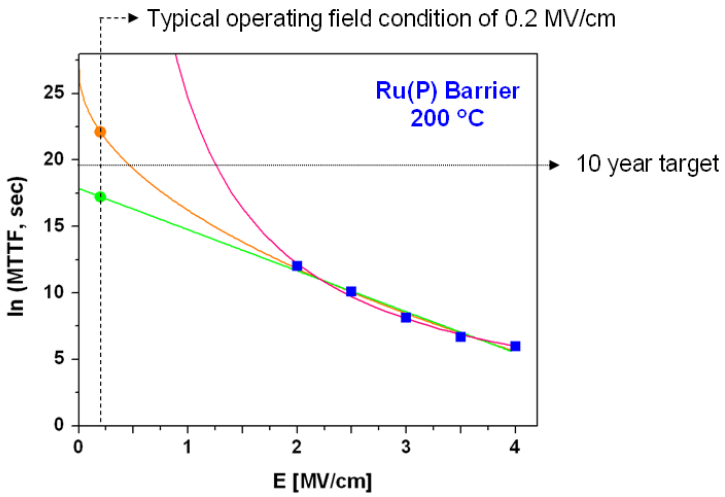


**Figure 2.5** The three time to failure models, compared to a failure test on an amorphous Ru(P) film at 25 at.% P. The 1/E trend-line is red, √E is orange, and E is green.

Since the capacitors are identical save for the barrier/liner layer, we can make the assumption that the differences observed in failure rates relate to the performance of the Ru alloy layer as a Cu diffusion barrier, and the third model is likely the most applicable under our conditions. The collected data itself is also useful for direct comparison of films without projection, as a film consistently longer in time to failure at high field stresses should also have a longer time to failure at lower stresses under the √E model.

## 2.3 REFERENCES

[1] Fadley, C.S.; J. Electron Spectroscopy and Related Phenomena 178 (2010) 2-32

[2] NIST X-ray Photoelectron Spectroscopy Database, 4.1 (NIST, Gaithersburg, 2012) and NIST X-Ray Mass attenuation Coefficients Database, Table 3, http://physics.nist.gov/PhysRefData/XrayMassCoef/ElemTab/z44.html

[3] C.D Wagner, et al. Surface Interface Anal. 3 (1981) 211

[4] R. Kwok, XPSPEAK 4.1, http://www.uksaf.org/software.html

[5] H. Okamoto, P-Ru, Binary Alloy Phase Diagrams 2nd ed. 3 (1990) 2978

[6] L. B. Henderson, J. G. Ekerdt, Thin solid Films 517 (2009) 1645-1649

# Chapter 3: Reducing the carbon content of Ru(P) films by using $PH_3$ as the phosphorus source

## 3.1 CHAPTER SUMMARY/ABSTRACT

In this chapter, The use of $PH_3$ as the P source in the growth of amorphous ruthenium-phosphorus alloy films by dual-source chemical vapor deposition (CVD) with $Ru_3(CO)_{12}$ to produce thin (~3nm) Cu diffusion barriers is examined. Comparisons are made to films grown using $P(CH_3)_3$. Carbon contamination of 10 at.% carbon or less was observed in $PH_3$-produced Ru(P) films, compared to greater than 30 at.% carbon in films using $P(CH_3)_3$, and $PH_3$-based Ru(P) films were also observed to have lower resistivity than $P(CH_3)_3$-based films. $PH_3$ was found to be much more reactive than previously-used P precursors, requiring the use of very low $PH_3$ partial pressures (~ 133 μPa) and a sequenced addition process that allowed accumulated P to diffuse into the Ru(P) film during growth. X-ray-refraction (XRR) and atomic force microscopy (AFM) indicate that films of good continuity and smoothness can be grown by CVD in the 3nm thickness range. X-ray diffraction shows the amorphous phase to be stable for annealing to 400°C for 3 hr. Electric field stress tests to failure for Cu/Ru(P)/$SiO_2$/Si stacks indicate that low-carbon Ru(P) barrier films function at least as well as their higher-carbon counterparts as Cu barriers and better than Ta/TaN stacks of similar thickness grown for comparison purposes.

The major findings of this chapter were published in Thin Solid Films (2014), 558 pp 160-164*.

---

* D. Bost, J.G. Ekerdt; Thin Solid Films 558 (2014) pp 160 - 164. Daniel Bost was the primary author.

## 3.2 GROWTH AND PRODUCTION OF LOW-CARBON FILMS

### 3.2.1 Carbon Content

Ru(P) films grown using $PH_3$ were found to have C contamination on the order of 10 at.% carbon (Figure 3.1), a large decrease compared to $P(CH_3)_3$-produced films, which had C content as high as 50 at.% or 60 at.% [1]. The 10 at.% incorporation level is also consistent with films grown from $Ru_3(CO)_{12}$ with no P precursor. There was also no perceived dependence of C content on P content or $PH_3$ partial pressure during growth, indicating that the observed C incorporation is independent of $PH_3$ pressure. This further indicates that the methyl ligands of $P(CH_3)_3$ are the major source of C contamination in Ru(P) films grown with $P(CH_3)_3$ and that low-C film growth is possible using the $PH_3$ source.

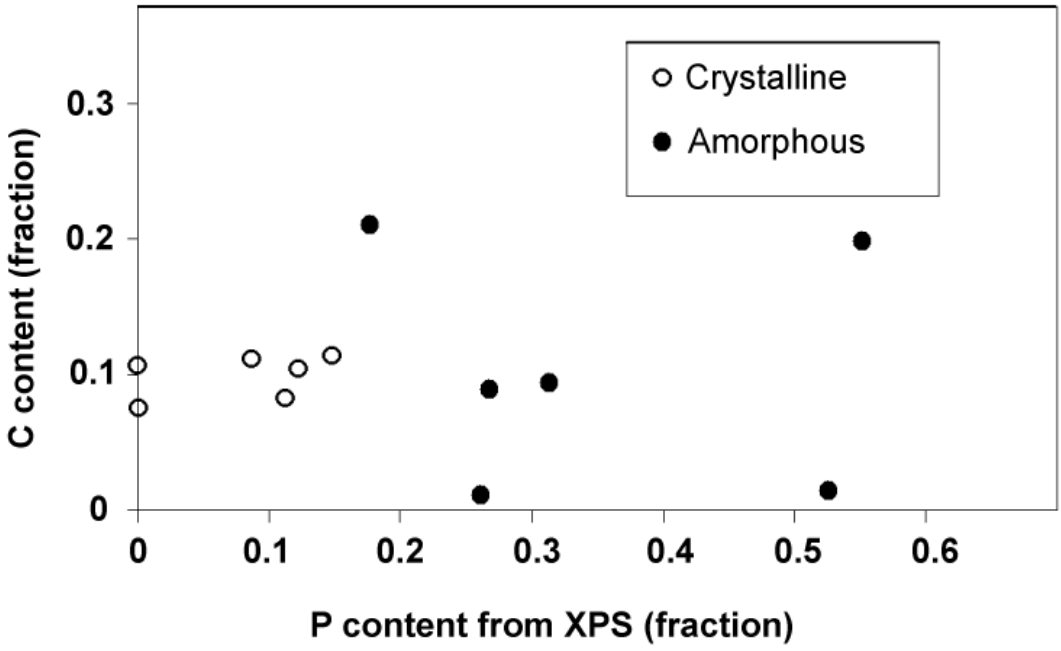


**Figure 3.1** Analysis of XPS data yields C contents on the order of 10 at.%, unaffected by P content for $PH_3$ films.

### 3.2.2 Managing P incorporation and Variation in Composition with Depth

$PH_3$ decomposed and incorporated into Ru films much more readily than $P(CH_3)_3$. While 1.3 Pa of $P(CH_3)_3$ produced films of 13-15 at.%, early attempts to grow films with 130 μPa $PH_3$ resulted in P contents as high as 70 at.% near the film surface, requiring that the $PH_3$ content of the precursor gas be reduced several times before a film of controllable P content could be produced.

Additionally, films grown with a constant partial pressure of $PH_3$ exhibited dramatic variations in composition across the thickness of the film, generally being as low as 10 at.% P near the Ru(P)/$SiO_2$ interface and increasing to as high as 50 to 70 at.% P over several nm of film thickness (Figure 3.2).

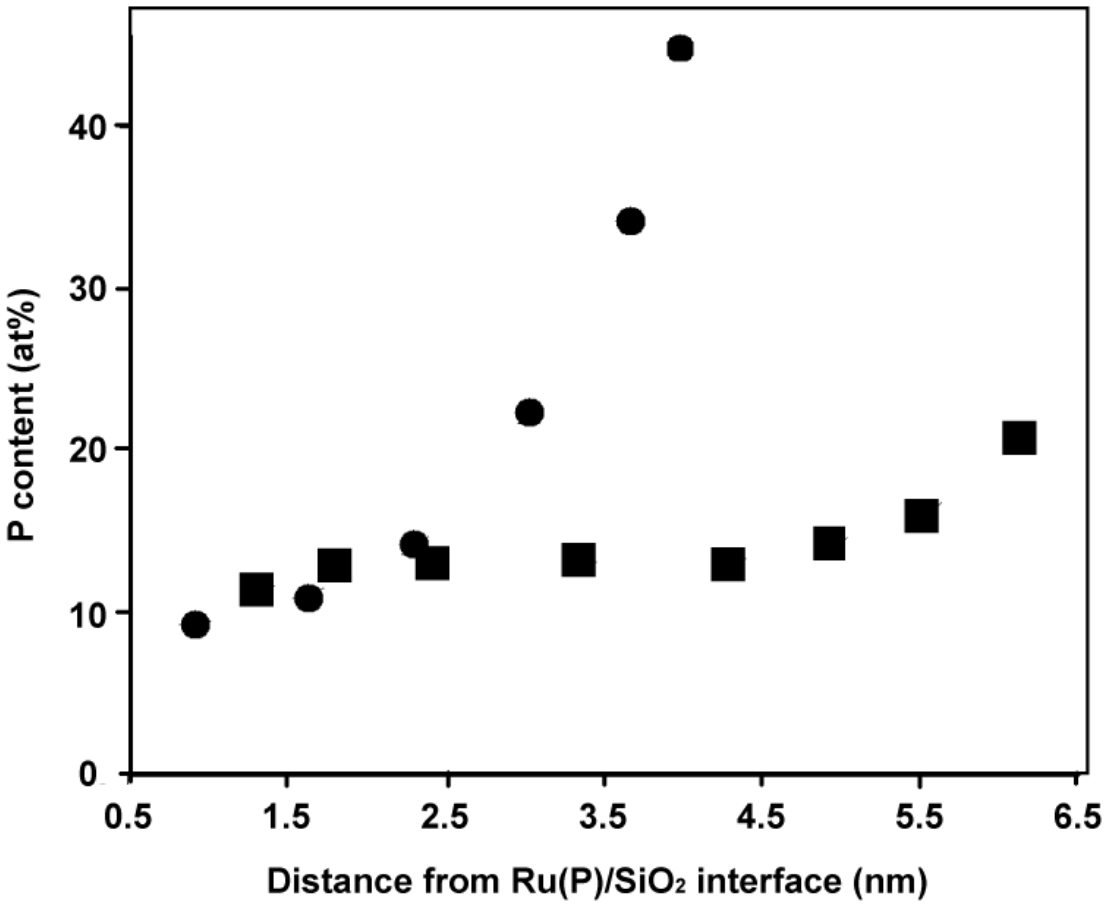


**Figure 3.2** Rapid P accumulation at the growth surface during deposition results in a dramatic increase in variation of P content vs film depth. The squares are a depth profile obtained from a constant $P(CH_3)_3$ pressure of 1.3 Pa during a 300 C CVD deposition. The circles are a similar, shorter deposition using 130 μPa $PH_3$.

This variation likely results from the decomposition of $PH_3$ on the Ru growth surface exceeding the rate of P incorporation into the film, in contrast to $P(CH_3)_3$-based growth where P likely incorporated as fast as the $P(CH_3)_3$ decomposition allows.

$P(CH_3)_3$ decomposes completely on Ru at 175°C, and $PH_3$ at -85°C [2], creating an accumulation of P at the growth surface with time, leading to an ever-increasing driving force for P incorporation that causes P content to monotonically increase from the Si/Ru(P) interface to the surface of the Ru(P) film.

The mobility of P in the grown and growing Ru(P) films was established by two tests. In the first, a 2 nm Ru film was grown on an $SiO_2$ substrate without any P precursor present, verified to lack detectable P by XPS, and then exposed to a constant pressure of 530 μPa of $PH_3$ for one hr at various temperatures near Ru film growth conditions. At both 300°C and 250°C the films showed a surface P concentration of 12 at.% and 8 at.%, respectively, following this treatment. XPS-based composition depth profiling showed measurable P content (3 at.% P) up to 0.5 nm (250°C) and 0.7 nm (300°C) below the exposed surface. This verified the ability of P from a $PH_3$ source to diffuse into already-deposited Ru from the growth surface.

In the second mobility test, a Ru(P) CVD film was grown for one hr in total at 250°C. For the first 15 min of growth, the film was exposed to $PH_3$ at a pressure of 530 mPa in addition to the Ru precursor. For the remaining 45 min the $PH_3$ partial pressure was reduced to 0 mPa, and the $PH_3$ source was isolated from the chamber completely. The $Ru_3CO_{12}/H_2$ mixture pressure was not altered during growth. The resulting profile (Figure 3.3) shows an increase from the bottom of the film for about 1.5 nm, then an abrupt drop from 35 at.% P to 17 at.% P, followed by a gradual falloff of P concentration to about 8 at.% P at the surface (~4 nm total thickness). This demonstrates the ability of the $PH_3$-produced P that accumulates near the surface during the initial exposure phase to segregate at the surface and incorporate into the growing film or diffuse through the parts of the film already deposited after the time of $PH_3$ exposure.

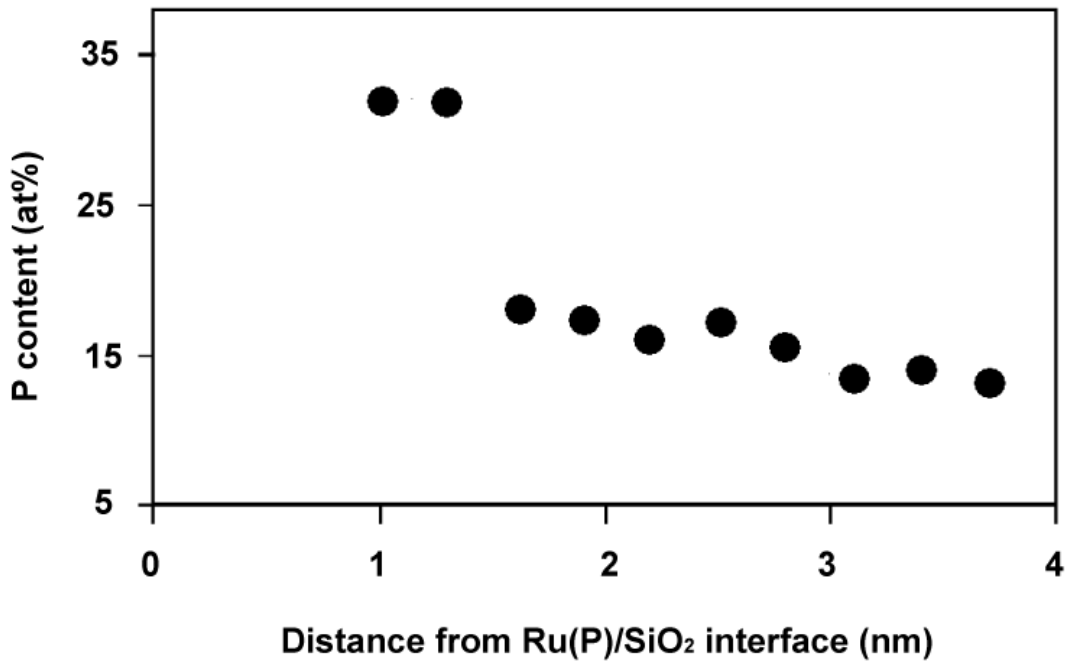


**Figure 3.3** A one-hour Ru(P) growth with the P source removed at 15 min.

The effect of substrate temperature on P mobility was examined by growing films at various temperatures and constant $PH_3$ pressure and examining their composition by XPS depth profiling. The slope of the P concentration curve was not found to change significantly when temperature was varied within the operating limits of the equipment and the $Ru_3CO_{12}$ used as a Ru precursor (200°C to roughly 500°C [3]). It was concluded that there was significant accumulation and migration of P in the Ru(P) under CVD growth conditions ranging from 200°C to roughly 500°C. However, within that temperature range varying the substrate temperature did not have a large enough effect on the composition profile to allow for uniform incorporation of P with film thickness.

A method of controlling the composition profile by varying the partial pressure of $PH_3$ during film growth was developed through extended trial and error to achieve films

with a variation of 5 at.% P over 3-4 nm of depth. Since the constant-$PH_3$ concentration profiles increased monotonically (Figure 3.2), we started with the general idea of decreasing the $PH_3$ input over the course of a growth run and varied the initial flow rate, step size and duration of the flow rate reductions, and final pressure of the $PH_3/H_2$ mixture until a set of conditions producing films of acceptable thickness, composition, and composition profile were produced. The final process developed starts with a relatively high dose, then decreases the $PH_3$ concentration in 2.5-min intervals, reaching zero some time before the end of the growth. An example is outlined in Figures 3.4 and 3.5.

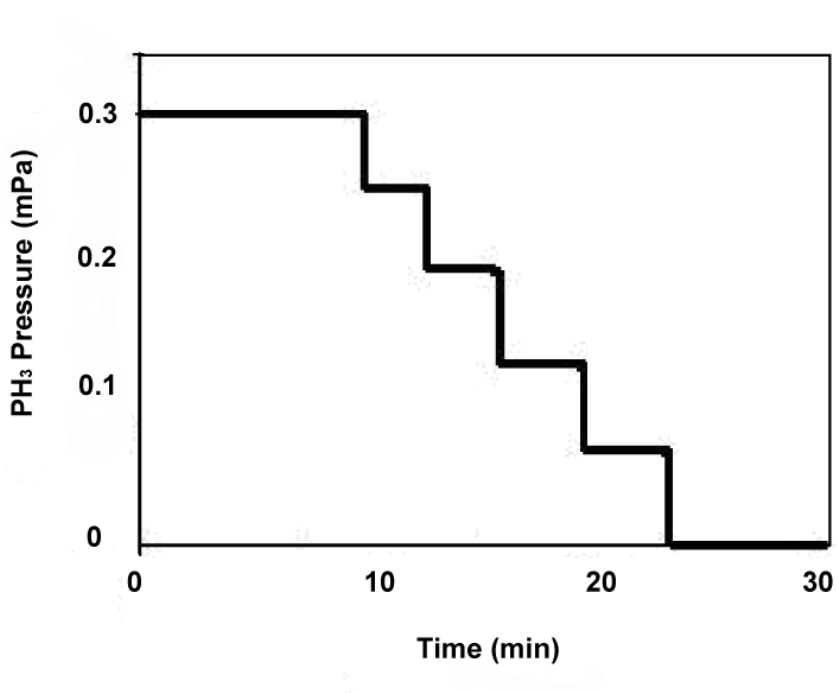


**Figure 3.4** To combat the rapid increase in P accumulation with time, the partial pressure of $PH_3$ is gradually decreased over the course of the deposition cycle.

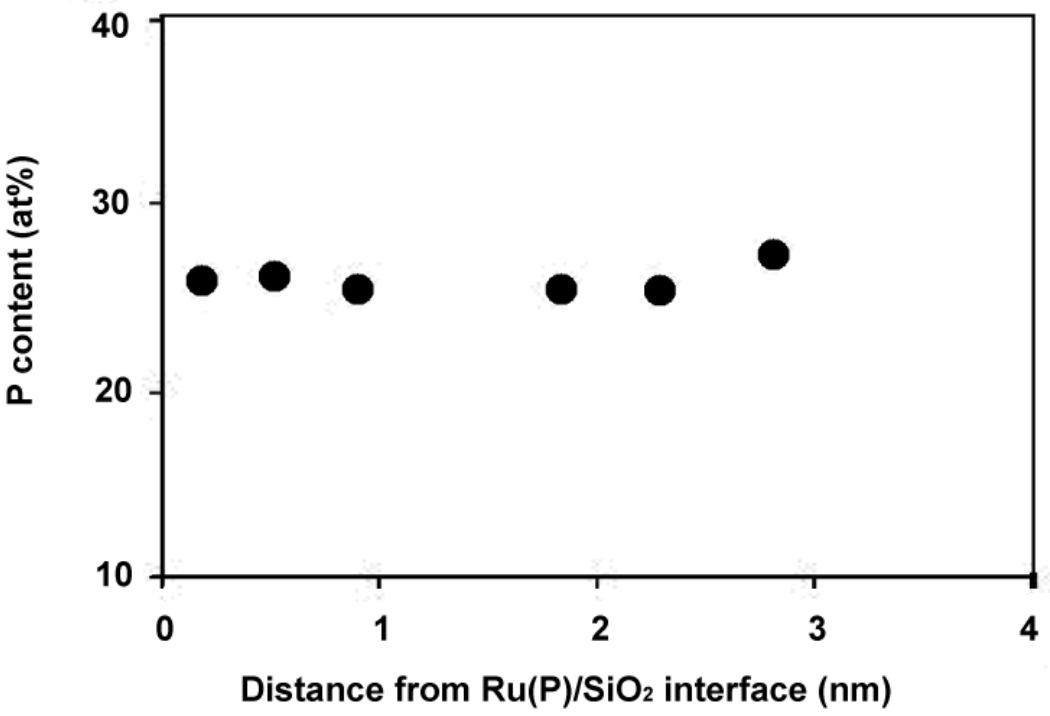


**Figure 3.5** The process outlined in Figure 3.4 results in a relatively unvarying concentration profile, allowing the growth of films that minimize excess surface P while retaining contents above the amorphization target of ~20 at.% P.

### 3.2.3 Film Structure and properties

The potential use of Ru(P) films as a Cu diffusion barrier/liner requires that they be as thin as possible while remaining continuous. Amorphous Ru(P) films grown for this study using $PH_3$ are consistently continuous at ~3 nm, with rms roughnesses of 0.02 - 0.22 nm, with the majority at about 0.1 nm. Thicknesses and a first assessment of smoothness were measured by XRR, verified by XPS attenuation, and finally examined

with AFM. If no evidence of discontinuity or film roughness on the order of film thickness was found, the film in question was judged continuous. $P(CH_3)_3$-grown CVD Ru(P) films have been reported in the 10 nm [1] and 5 nm [4] thickness ranges. $PH_3$ films at or below 2 nm could not be produced with consistent continuity by our equipment/process, exhibiting rms roughnesses on the order of 1-2 nm in AFM and giving no reliable signal for thickness estimation in XRR (a sign of high roughness). Similarly, films that were not amorphous (generally <17 at.% P) were frequently not continuous even at the 3 nm target thickness.

The amorphous nature of the Ru(P) system is one of the primary reasons that it is potentially a Cu diffusion barrier candidate. By examining the films in XRD and comparing to the substrate signal and known crystalline XRD profiles for Ru and the various $Ru_xP_y$ crystal structures, the crystallinity or amorphous character of films were determined. Ru(P) films as-grown were found to be consistently amorphous above 20 at.% P and consistently crystalline below 17 at.% P (Figure 3.1). This matches first-principles modeling predictions [1]. By comparison, $P(CH_3)_3$-grown Ru(P) films were sometimes amorphous as low as 15 at.% P, probably as a result of higher C content.

To test stability under annealing, several amorphous Ru(P) films of 3 nm thickness were annealed at 400°C and 450°C as described in Section 2.3.2 for 3 hr per anneal. It was found that films of 20 at.% P to 30 at.% P had an amorphous phase stable at 400°C, but at 450°C they began to crystallize, showing the characteristic structure of Ru (Figure 3.6). $P(CH_3)_3$-grown Ru(P) films were found to be stable at 450°C and crystallize at 500°C.

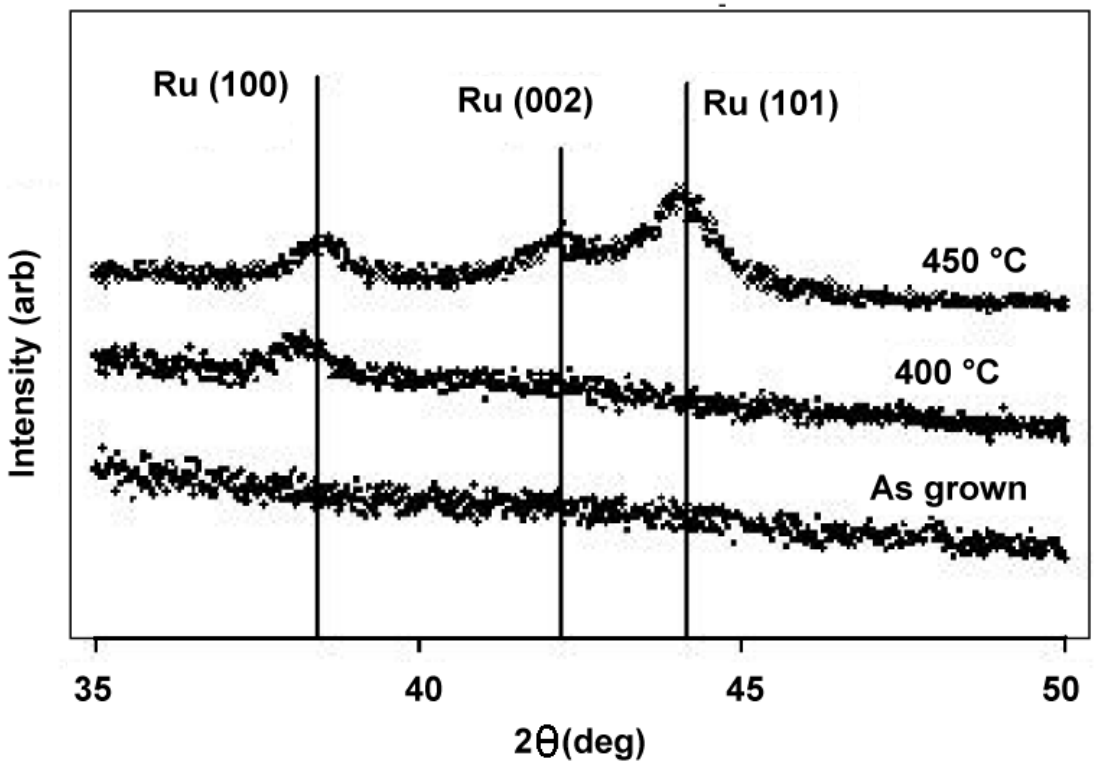


**Figure 3.6** A sample anneal to crystallization. This 3-nm Ru(P) film had 25 at.% P and was continuous as-grown.

Direct examination of sheet resistance using a 4-point probe and XRR- and XPS attenuation-calculated thicknesses allows the direct examination of film resistivity in various Ru(P) films, shown in Figure 3.7. While low-C films had a lower resistivity than $P(CH_3)_3$-grown films of similar composition in the 15 at.% to 25 at.% P range, we note a strong dependence on P concentration, with film resistivity increasing significantly with P concentration. Thus, keeping P concentration near the 20 at.% amorphization threshold remains an important concern for the liner application.

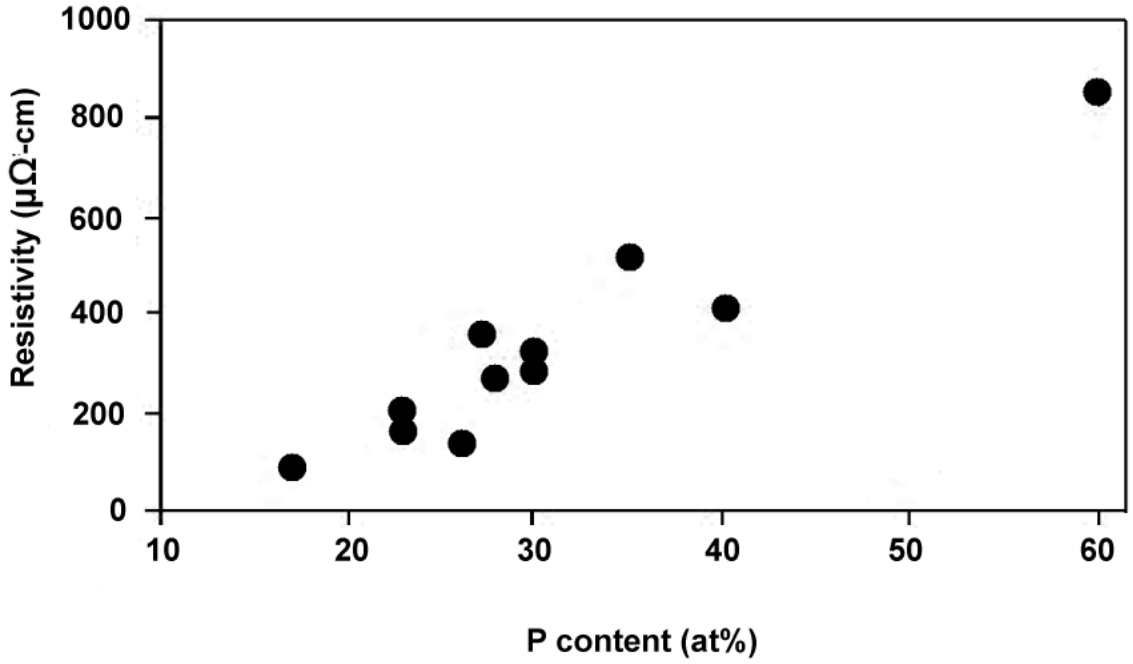


**Figure 3.7** The resistivity of Ru(P) films increases with increased P content.

It is further worthy of note that the films shown in Fig. 3.7 are all in the 3 to 4 nm thickness range. Pure Ru at this thickness (grown by ALD for continuity) has been measured at 50 to 80 μΩ-cm [5], which is higher than the listed bulk resistivity of Ru due to dimensional constriction [6]. The resistivities of the films near the 20 at.% to 25 at.% compositions (in the 100 to 200 μΩ-cm range) are slightly higher than pure films at these thicknesses due to P acting as an impurity impeding electrical conduction.

### 3.2.4 Barrier Performance

The procedure outlined in Chapter 2, Section 2.2.8 was used to test the operational lifetime of the low-C Ru(P) films. The basis for this test and methods for extrapolating these performance lifetimes to actual operating conditions are explored in

Reference [4] and [7]. The two dominant models for field-stress barrier failure predict that log(time to failure) is a linear function of either the field strength or its square root, allowing tests to failure at a very strong electrical field to stand in for years-long tests at operational voltages. This chapter seeks to compare the films against their high-C counterparts and a sample TaN film grown using the in-house PVD equipment.

The film examined was a 3 nm low-C Ru(P) CVD film with 25 at.% P, with 2 nm of Ru grown on top of it by PVD. The addition of the PVD layer was solely to bring the total thickness to 5nm, in order to keep the thickness consistent with the high-C and TaN samples to which it was to be compared. Figure 3.8 presents the raw data for the test, and Figure 3.9 presents the median at each load superimposed on similar median lines for the high-C PVD Ru(P) and the PVD TaN. The performance under field stress for the low-C films is very similar to that of the high-C films, showing it to be of similar overall viability as a Cu barrier material even in the absence of additional carbon in the material beyond the 10 at.% or less accumulated from background growth effects.

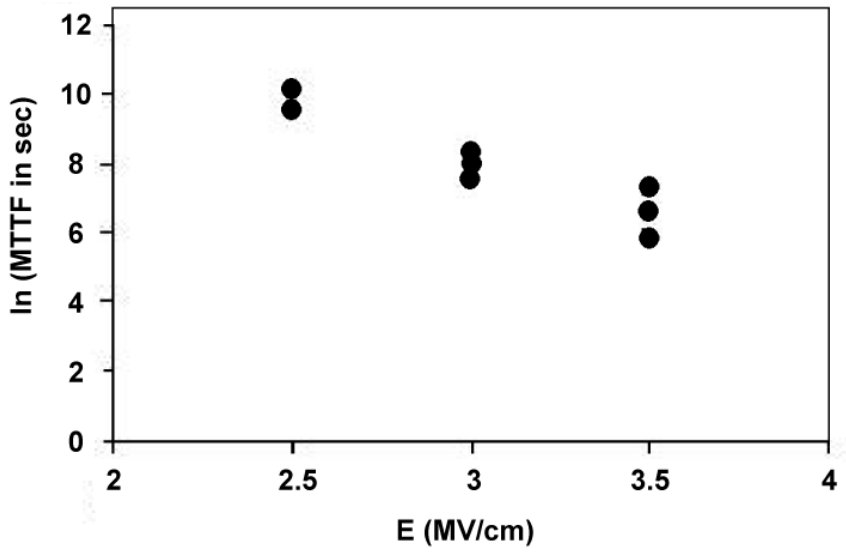


**Figure 3.8** Pre-averaged data for the low-C Ru(P) film (6 at.% C), giving some idea of the error bars involved in TTF measurements.

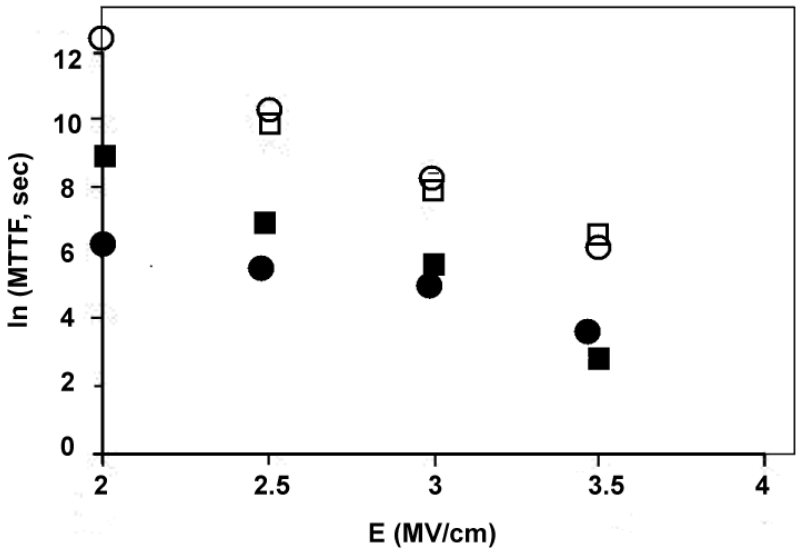


**Figure 3.9** Time to failure versus field strength for various films; ■ is a 5 nm TaN film grown for comparison purposes, □ is a low-C Ru(P) film (25 at.%P) grown with $PH_3$; ○ is a high-C Ru(P) film (20 at.%P) grown with $P(CH_3)_3$; and, ● is a 5 nm Ru crystalline film with no P.

Extrapolation of these results using the √E model of dielectric failure as outlined in Chapter 2, which assumes a failure related to copper diffusion, can be used to provide a rough approximation of the films' impact on device lifetimes at field stresses more typical of normal use. At 200 V/cm it predicts a time to failure in excess of a century, indicating that the film's performance as a barrier is sufficient to not be the limiting factor on device lifetime.

### 3.3 THE BARRIER/LINER APPLICATION

$PH_3$ is a challenging precursor material for Ru(P) CVD due to its high reactivity, but when properly handled it produces films of dramatically lower C content than $P(CH_3)_3$. Even in the relative absence of carbon, amorphous metallic thin films can retain their metallic character and continuity at thicknesses as low as 3 nm.

While continuity, low resistivity, and a stable amorphous phase are good indicators of the viability of $PH_3$-grown low-C Ru(P) films for use as interconnect liners/Cu diffusion barriers, it is good to also have a quantitative grounds for comparison of performance with other materials under field stress, and the time-to-failure stress test described above continues to provide a viable means for such comparisons, giving us a direct indicator that low-C Ru(P) films may serve well in the interconnect liner/barrier application.

### 3.4 REFERENCES:

[1] J. Shin, H.-W. Kim, G. S. Hwang, J. G. Ekerdt, Sur.Coat. Tech. 201 (2007) 9256

[2] J.-H.Shin, H.-W.Kim, K.Agapiou, et al., J. Vac. Sci. Tech., A26 (2008) 974

[3] J. Paschool, H. Kleykamp, F Thummler, J. Less Common Met. 98 (1984) 279

[4] L. B. Henderson, J. G. Ekerdt, Thin Solid Films 517 (2009) 1645

[5] Li et al., Journ. Electrochem. Soc. 154(12) (2007) D642-D647

[6] Fuchs, K.; Mott, N. F., Proc. of the Cambridge Philos. Soc., 34(01) (1938), p.100

[7] G. Raghavan, C. Chiang, et al., TSF 262 (1995) 168-176

# Chapter 4: Ruthenium-Boron Alloy thin films

## 4.1 CHAPTER SUMMARY/ABSTRACT

The growth of ultrathin (3-nm) amorphous Ru(B) alloy films of varying B concentration via chemical vapor deposition is explored using $Ru_3(CO)_{12}$ and $B_2H_6$ as the Ru and B sources, respectively. Experiments reveal the films grown at 250 °C are amorphous at B contents in excess of 15 at.% and polycrystalline below 10 at.% B, consistent with first-principles predictions. Amorphous Ru(B) films remain amorphous following annealing at 450 °C and become polycrystalline at 500 °C. Film resistivity ranged from 40 to 120 μΩ-cm and was independent of B loading, and film roughness was <0.2 nm rms roughness for 3-nm-thick films. Electric field stress tests to failure for Cu/3-nm Ru(B)/$SiO_2$/Si stacks are used to indicate suitability of Ru(B) as a copper diffusion barrier layer.

The contents of this chapter reflect D. Bost's contributions to "First-principles predictions of ruthenium-phosphorus and ruthenium-boron glassy structures and chemical vapor deposition of thin amorphous ruthenium-boron alloy films"†, published in Thin Solid Films 662 (January 2017) pages 56 - 64 [1].

† D. Bost, H-W Kim, C-Y Chou, G.S. Hwang, J.G. Ekerdt, Thin Solid Films 662 (2017) 56 - 64. Daniel Bost was the primary author.

## 4.2 Growth and Production of Ru(B) Films

### 4.2.1 Film Growth using $B_2H_6$ as a B source in Ru(B) CVD

As with the $PH_3$ used in low-carbon Ru(P) film growth in Chapter 3, $B_2H_6$ tends to rapidly and completely decompose on Ru and Ru(B) under growth conditions, resulting in a much higher B content in the films for a similar concentration of gas during growth as with $PH_3$. This is expected since $B_2H_6$ is reported to decompose completely on Ru at 100 °C [2] and each $B_2H_6$ molecule supplies two B atoms. In practical terms the high reactivity presents challenges to limit the incorporation levels of B into the film during growth. The 15 ppm $B_2H_6$ source concentration used here was chosen because it was the lowest concentration commonly sold by the manufacturer, and control of composition relied on adjustments of B source gas flow rate on the order of 0.2 sccm, toward the lower limits of the mass flow controller precision. Other CVD chambers will need to establish protocols for limiting and regulating the partial pressure to very low levels.

In another similarity to Ru(P) grown with $PH_3$, $B_2H_6$-produced B accumulates on the growth surface more rapidly than it can be incorporated by the growing Ru(B) film, resulting in a steeply increasing B concentration moving away from the Ru(B)/$SiO_2$ interface to the growth surface if the $B_2H_6$ partial pressure is kept static during growth. To keep the film composition uniform with thickness the $B_2H_6$ partial pressure in the CVD chamber was varied over the course of the growth cycle for each film, beginning high and then gradually stepped down to zero over the course of film growth (shown in Figure 4.1 for a film grown at 250 °C). Figure 4.2 presents the concentration profile corresponding to the pressure settings in Figure 4.1. There is less than 5 at.% variation in the calculated B content of the film over three nm of total film thickness. The specifics of the concentration step size and times were based on, previous work with phosphorus-

source CVD of Ru(P) reported in Chapter 3 and were found to produce a low variation in mean B concentration with position relative to the Ru(B)/$SiO_2$ interface. Overall film composition is reported using a mean B concentration. The reported B concentrations vary by no more than +/- 2.5 at.% B from the reported average composition at any measured depth within the film; films with any readings outside this range were considered too inconsistent in composition for further use.

Films were grown at substrate temperatures of 250 °C, 300 °C, and 350 °C, and no dependence in B the concentration profile was observed within this temperature range. This was expected since $B_2H_6$ decomposes on Ru at a much lower temperature (decomposition has been observed at -25 °C and complete decomposition at 100 °C [2]) than the lower limits of the $Ru_3(CO)_{12}$ ruthenium precursor deposition temperature (150 °C). [3] A substrate temperature of 250 °C was used for all films reported herein.

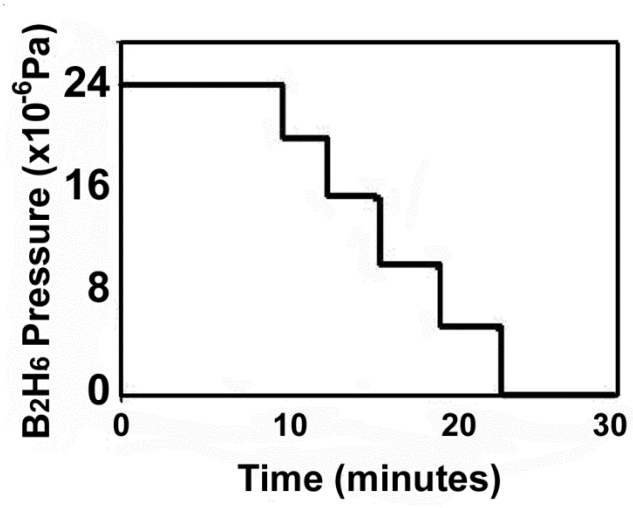


**Figure 4.1** Partial pressure of diborane was decreased in regular steps of 2.5 minutes following an initial higher exposure.

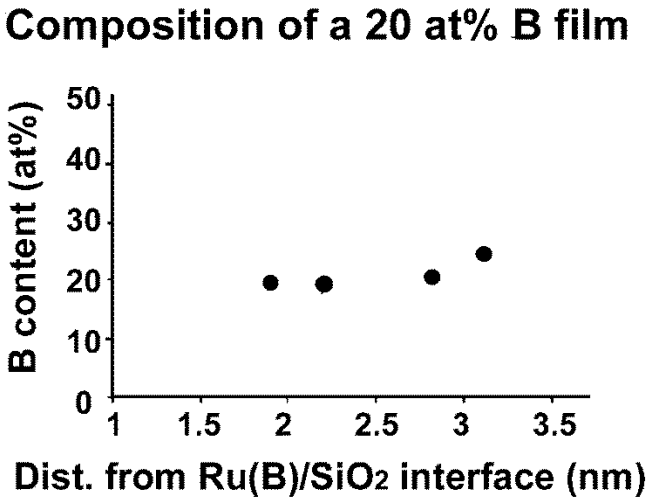


**Figure 4.2** This composition profile was obtained from XPS analysis of the film grown in Figure 4.1; there is still some variation in the B content but it was reported as the average (20 at.% B). All films grown had this +/-2 at.% variation.

### 4.2.2 Carbon content, resistivity, and surface oxidation of B

The carbon content of the films was monitored, and as with low-carbon Ru(P) films reported in Chapter 3 the Ru(B) CVD films grown with a hydride source, $B_2H_6$, were found to have C contents between 0 and 10 at.%. The likely source of C contamination is the carbonyl ligands in the $Ru_3(CO)_{12}$ precursor.

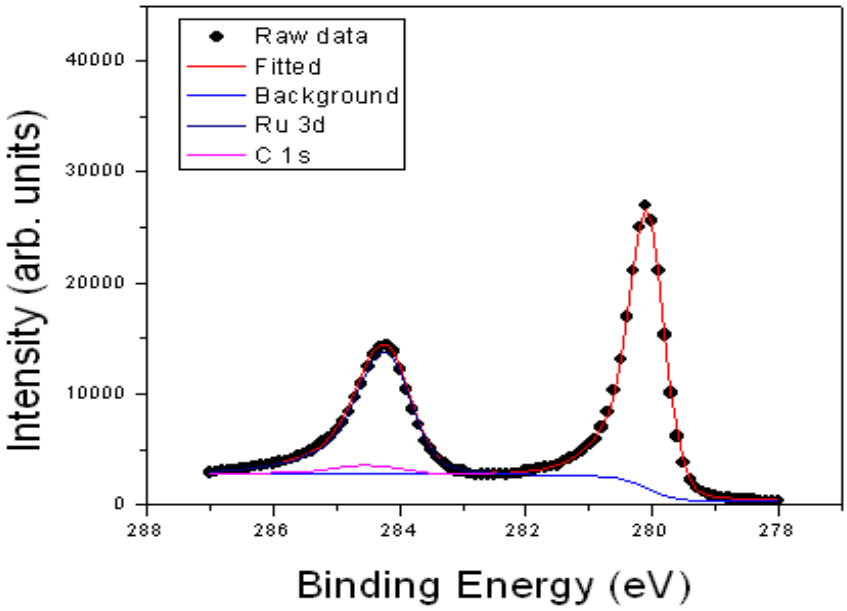


**Figure 4.3** Deconvolution of the C 1*s* peak for a sample with ~30 at.% C

An additional concern for platability is potential oxidation of alloy components at the surface of the film, which might have an adverse effect on Cu platability. XPS peak analysis of the Ru(B) films was done *in situ*, but often following several hours of cooling and transportation under vacuum following growth. XPS Ru 3*d* peaks were consistent with zero-valent ruthenium, but often a secondary boron peak was observed at 193 to 193 eV, consistent with known B oxides, in addition to the zero-valent B 1*s* peak at 189.4 eV (see Figure 4.4). This signal disappears following any amount of sputtering (as little as 0.05 nm equivalent of sputter time) so the oxidation is limited to the boron on the film surface, and may not present an insurmountable obstacle to processing.

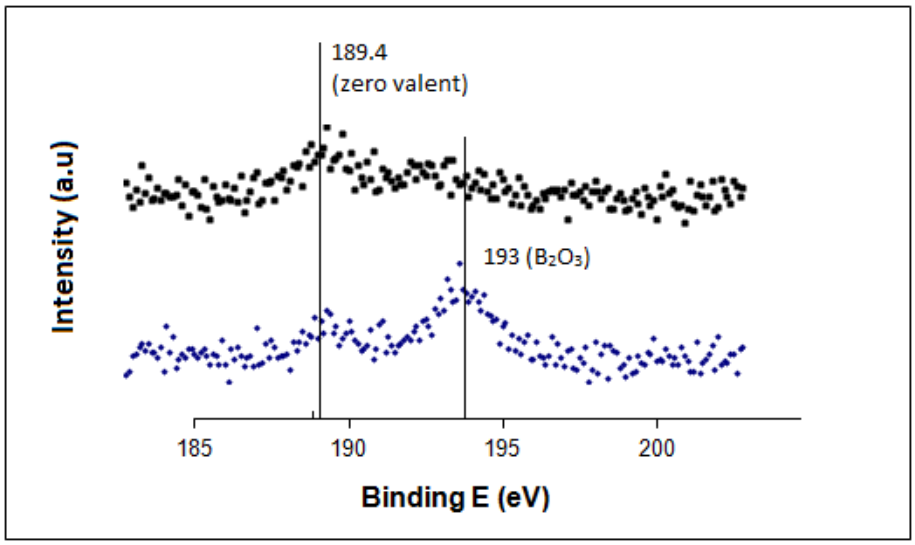


**Figure 4.4** A comparison of the B 1*s* XPS spectra of the oxidized surface of a 15 at.% B Ru(B) alloy film exposed to oxygen in the course of sample transfer (bottom) and the same sample after 20 seconds of Ar+ plasma sputter etching (top), which removes less than 0.1 nm of material from the alloy film.

Another important concern for Ru(B) alloy films in a Cu diffusion barrier application is the reproducibility and stability of the amorphous phase. First-principles predictions suggest thin Ru(B) films will be amorphous above 10 at.% B and polycrystalline below 10 at.% [4]. Figures 4.5 and 4.6 show representative XRD spectra for films grown below and above this threshold, respectively. The low sensitivity of the B 1*s* signal in XPS (sensitivity factor 0.13) makes it difficult to quantify concentrations below 10 at.% B whereas concentrations above 10 at.% B can be quantified with an estimated uncertainty of +/- 2.5 at.% B. Films below the 10 at.% B threshold were observed to have resistivities varying between 30 and 120 μΩ-cm (not shown on Figure 4.7 due to inability to quantify the B content). All films shown in Figure 4.7 are 3 nm thick and were grown at 250 °C. In general Ru(B) films in excess of 10 at.% B were

found to be consistently amorphous; almost all Ru(B) films in the 10-15 at.% B range were amorphous as grown, and films above 15 at.% B were amorphous. Ru(B) films below the 10 at.% B threshold were found to be polycrystalline, exhibiting the diffraction features of pure Ru XRD.

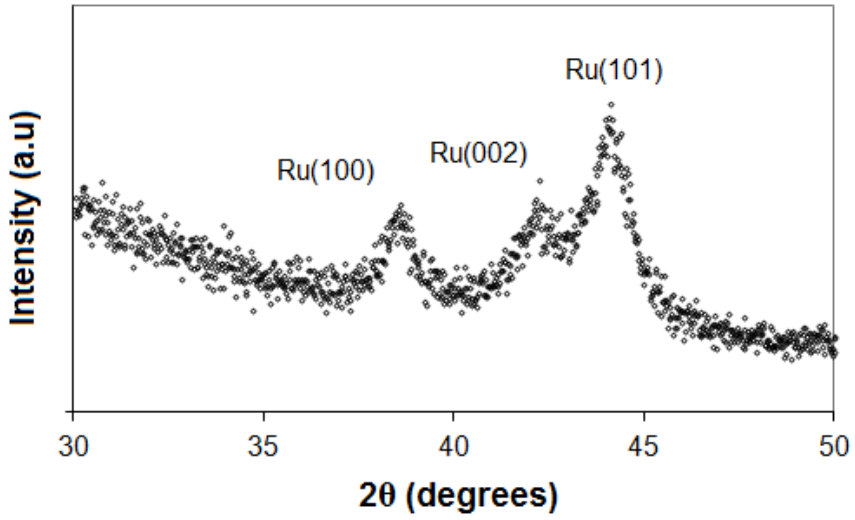


**Figure 4.5** XRD of a < 10 at.% B Ru(B) alloy film (3-nm thickness), exhibiting strong Ru crystal structure features.

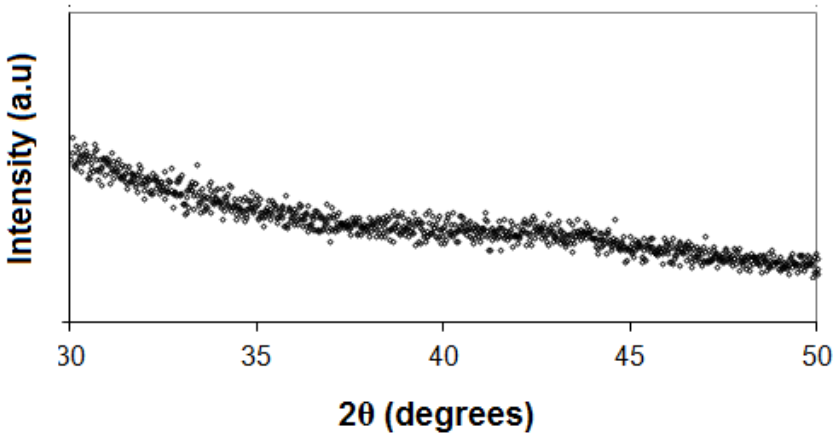


**Figure 4.6** XRD of a 3-nm 15 at.% B Ru(B) alloy film

Figure 4.7 presents the resistivity of 3 nm Ru(B) films (obtained by measuring sheet resistance of films with a 4-point probe). There is no discernible trend in resistivity with B content, with the highest resistivity recorded at 120 μΩ-cm. These values are similar to those of Ru(P) films below 25 at.% P in Chapter 3. These results are higher than the known bulk resistivity of pure Ru, and are close to thin film single-crystalline Ru resistivity at similar thicknesses due to the effects of dimensional restriction (50 to 80 μΩ-cm) [5, 6].

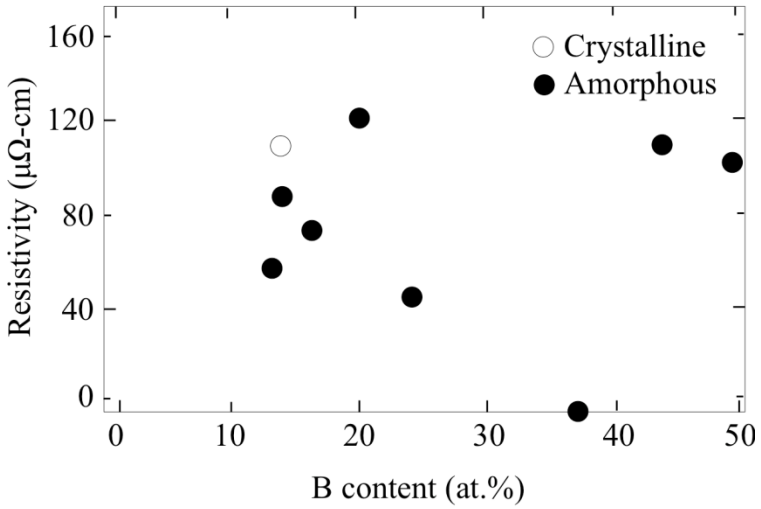


**Figure 4.7** No correlation between resistivity and B content was observed.

### 4.2.3 Film roughness and Temperature Stability

Atomic force microscopy (AFM) was used to measure the roughness of various 3-nm amorphous Ru(B) films (Table 4.1 shows a representative AFM result for a continuous and discontinuous film). RMS roughness of films found to be continuous was on average approximately 0.1 nm, +/- 0.05 nm, which is similar to Ru(P) amorphous

films of similar thickness reported in Chapter 3. Attempts to produce films at lower than 3-nm thickness with our equipment and techniques resulted in observed discontinuities and large rms roughnesses indicating that the films were not continuous.

| Sample Name | rms (first run) | rms (second) | rms (third) | avg |
|---|---|---|---|---|
| RuB57 | 0.215 | 0.104 | 0.141 | 0.153 nm |
| RuB61 | 2.11 | 1.95 | 2.00 | 2.02 |

**Table 4.1** The first sample was 3.2 nm thick and judged continuous. The second was an attempt to grow a film 2.5-nm in thickness, which was found to be discontinuous.

Temperature stability of the Ru(B) amorphous films was evaluated by alternating 3-hour anneals of Ru(B) films with x-ray diffraction analysis. Four films were tested, all 3-nm Ru(B) CVD grown at 250 °C, one with 13 at.% B, two with 15 at.% B, and one with 20 at.%B. Each film was amorphous as-grown, and checked for crystallization following a 300 °C anneal, then a 400, 450, and 500 °C anneal in sequence. Representative results are shown in Figure 4.8. Each annealing step maintained the relevant temperature at the film surface for two hours. All three films remained amorphous through the first three anneal cycles, and all three exhibited diffraction features associated with the Ru crystal structure following the 500 °C anneal. This is similar to the recrystallization of 3nm Ru(P) amorphous films in Chapter 3, which was found to occur following a similar 450 °C anneal (shown in Figure 4.9).

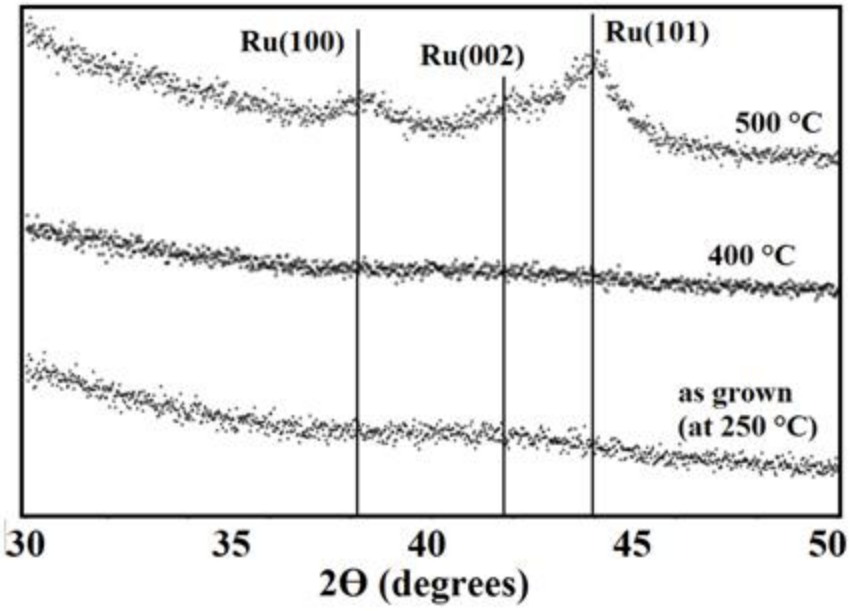


**Figure 4.8** Annealing of the 15 at.%B Ru(B) film in section 4.2.3.

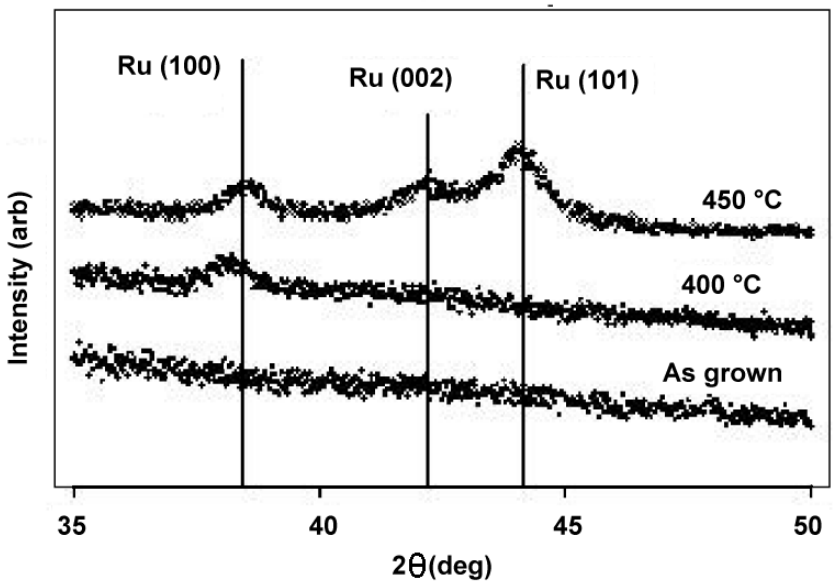


**Figure 4.9** The corresponding anneal to crystallization of a 3-nm film, 25 at.% P (also seen in Chapter 3, reproduced here for ease of comparison).

### 4.2.4 Barrier performance and comparison to amorphous Ru(P)

The electrical failure test described in Experimental Methods was performed on several 3-nm Ru(B) films, primarily to provide a direct comparison to the performance of previously-studied Ru(P) ultrathin films for use as liners and a 5-nm Ta/TaN stack produced using in-house PVD in the study in Reference 7. Further discussion of the method and previous related work can be found in several of the references [7, 8] and in Chapters 2 and 3. Three films were tested: a 15 at.% B film grown at 3 nm, a similar 15 at. % B film plated with an additional 2 nm of PVD Ru to bring its overall thickness up to 5 nm to allow direct comparison to earlier Ru(P) results [7, Chapter 3], and a 3-nm 25 at.% B film to provide an idea of whether increasing B content beyond the point where Ru(B) grows as an amorphous film provides any benefit to the Cu diffusion barrier application.

Figure 4.10 shows only the two 3-nm films because the additional Ru thickness added by PVD made no discernible difference in performance for the 15 at.% B films, and Figure 4.11 shows only the first film (15 at.% B, 3-nm) for visual clarity. We found there is not an substantial difference in performance between the tested films and the Ru(P) films evaluated in Chapter 3, shown in Figure 4.12, but they perform better than Ta/TaN stacks grown by PVD for rough comparison in previous work and polycrystalline Ru grown without alloying elements at 5-nm thickness. The Ta/TaN stack is 5-nm thick and does not truly constitute the current state of Ta/TaN Cu diffusion barrier layers in industry, but gives us some grounds for direct comparison of the materials due the testing stack being otherwise identical and produced using the same equipment. As with the films in Chapter 3, extrapolation of the trend using the $\sqrt{E}$ model results in a predicted

time to failure at 0.2 MV/cm in excess of a century, indicating that Cu diffusion across Ru(B) amorphous barrier layers in a device using such films is unlikely to be the cause of device failure.

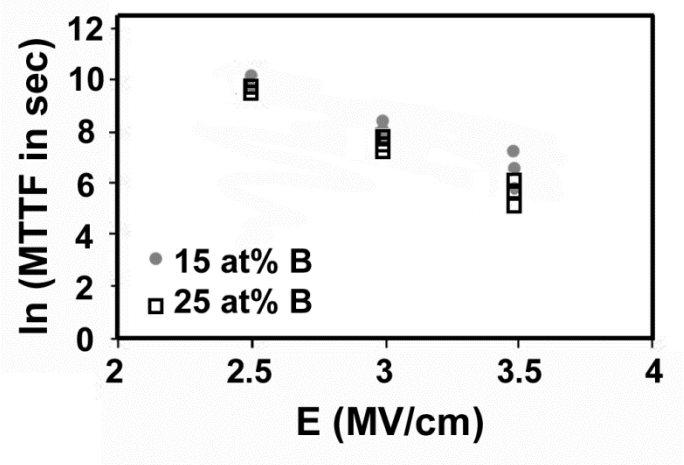


**Figure 4.10** The two tests shown are the 3nm Ru(B) films in section 4.2.4

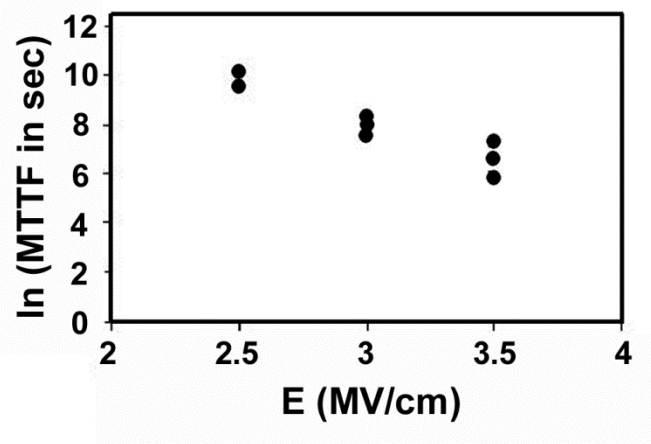


**Figure 4.11** The 15 at.% B results without the second sample for clarity.

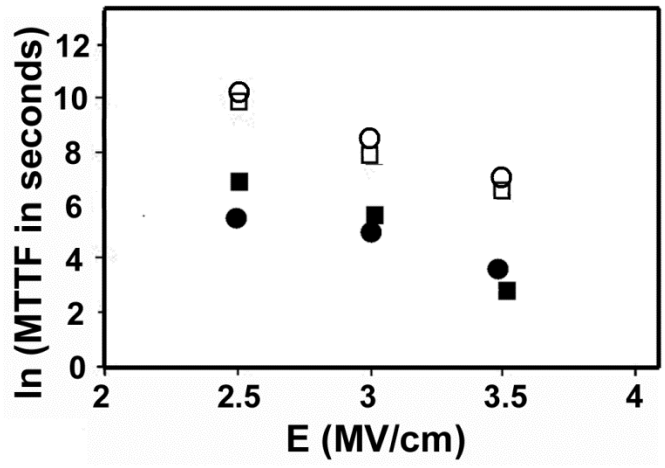


**Figure 4.12** □ is the median failure time of the 3nm 15 at.% B Ru(B) film. ○ is a 3-nm amorphous Ru(P) film reported in Chapter 3. ● is a 5-nm Ru crystalline film with no P, grown for comparison in Chapter 3, ■ is a 5-nm TaN film grown for comparison in reference [7].

### 4.3 THE BARRIER/LINER APPLICATION

Empirical testing of $B_2H_6$ used to grow Ru(B) amorphous films with CVD shows that it should perform very well as a platable ultrathin Cu diffusion barrier. Low film resistivity (<120 μΩ-cm), good continuity and smoothness at 3-nm thickness, and performance under failure testing and annealing all make it a strong contender for a liner material at low device node sizes. Performance equals or exceeds previously studied Ru(P) amorphous films, and the Ru(B) films require a lower concentration of precursors with no processing complications beyond those observed working with other hydride precursors.

**4.4 REFERENCES:**

[1] D. Bost, H-W Kim, C-Y Chou, G.S. Hwang, J.G. Ekerdt, Thin Solid Films 662 (2017) 56 - 64

[2] J. Rodriguez, C. Truong, J. Corneille, D. Goodman, J. Phys Chem, 96 (1992) 334-341

[3] H. Kim, S-H Lee, WT Lee, S Ganguli, H-C Ha, SH Yu, US Patent 20130146468 (2013) 2

[4] Hyun Woo Kim, "Structure and properties of amorphous metallic alloys: a first principles study", PhD dissertation, University of Texas Austin, OCLC 700073548 (2010)

[5] H. Li, D.B. Farmer, R.G. Gordon, Y. Lin, J. Vlassak, J. Electrochem. Soc. 154(12) (2007) D642-47.

[6] K. Fuchs, N.F. Mott, Proc. Cambridge Philos. Soc., 34(01) (1938), 100-108.

[7] L.B. Henderson, J.G. Ekerdt, Thin Solid Films 517 (2009) 1645 - 1649.

[8] G. Raghavan, C. Chiang, P.B. Anders, S-M Tzeng, R. Villasol, G. Bai, M. Bohr, D.B. Fraser, Thin Solid Films 262 (1995) 168-76.

# Chapter 5: Research Summary

## 5.1 Summary of Results

Two amorphous ruthenium alloys were examined for their general properties and use in potential Cu interconnect applications as an ultrathin (<5-nm) diffusion barrier. Smooth, continuous films of amorphous Ru(P) and Ru(B) were consistently grown at ~3-nm thickness using $PH_3$ and $B_2H_6$ respectively as the alloying element source in a two-source chemical vapor deposition at 250 °C, where $Ru_3(CO)_{12}$ was the ruthenium source. The concentrations of B and P in the films required to ensure they were amorphous was consistent with first-principles calculations: ~10 at.% B for Ru(B) and ~20 at.% P for Ru(P) were the concentrations above which the films were predicted to be amorphous. Ru(B) films known to contain less than 10 at.% B were consistently found to be polycrystalline and those containing more to be amorphous. Ru(P) films were found to be consistently amorphous if they contained more than 20 at.% P and consistently polycrystalline if they contained less than 18 at.% P.

Hydride-grown Ru(P) films were compared to films grown with $P(CH_3)_3$ and found to have a C content on the order of 10 at.% C compared to the "high-carbon" Ru(P) films often hitting or exceeding 30 at.% C. This verified earlier suppositions that the primary source of carbon contamination in the high-carbon films was the methyl groups on the P precursor (and the phenyl groups on earlier P sources used in CVD). Low-carbon Ru(P) proved to be more consistent with the first-principles models than its high-carbon predecessor, which became consistently amorphous as low as 17 at.% P due to the additional carbon. The low-carbon Ru(P) also exhibited lower resistivity (100 to 200 μΩ-cm at 20 to 25 at.% P) than high-carbon Ru(P) (500 to 2000 μΩ-cm), though increases in P concentration beyond the necessary 20 at.% P for amorphization was seen to increase film resistivity significantly (as high as 700 μΩ-cm at 50 at.% P).

Ru(B) was found to have both consistently lower resistivity than low-carbon Ru(P) (40 to 100 μΩ-cm) and no observed increase in resistivity with increased B concentration in the film.

Both low-carbon films were tested under electrical stress to failure using an MIS capacitor stack with the film as the isolator layer, and found to compare favorably to unalloyed Ru in barrier performance, as well as to a Ta/TaN stack used in previous work. Neither alloy obviously outperformed the other in this test.

## 5.2 CONCLUSIONS

The overall conclusion is that both Ru(B) and Ru(P) amorphous thin films grown with hydride gas alloying element sources are highly suitable for the Cu diffusion barrier application, with Ru(B) having a slight edge due to its lower resistivity and lower sensitivity to film composition. In the absence of excess carbon, both alloys have a resistivity that is similar to that of single-crystalline Ru in the same thickness range and can be produced in smooth, continuous layers at 3-nm thickness at the predicted concentration of alloying elements.

Of the two alloys, the Ru(B) films are slightly more stable under annealing; at 500 °C to Ru(P)'s 450 °C recrystalization temperature for films of corresponding compositions within 5 at.% of the minimum necessary concentration of the alloying element. Added to the tendency of the Ru(P) amorphous alloy to increase significantly in resistivity with at.% P, this makes amorphous Ru(B) slightly preferable for use in the Cu diffusion barrier application.

## 5.2 Recommendations for Future Work

The success of the hydride precursors in reducing carbon contamination, and the improvement of film properties with lowered carbon content, immediately suggests the use of hydride gas precursors for other materials of interest, such as Co(P), which has a wide variety of potential applications due to its magnetic and electrical properties.

The problems encountered in attempting to produce films of even composition across the entire film also indicate that accumulation of the alloying element on the growth surface is occurring at a different rate than alloying element incorporation for both $PH_3$ and $B_2H_6$. While this has no immediately obvious application to microelectronic devices or interconnect, further examination of this growth mechanism and films of non-uniform composition is of interest to the subject of thin films in general.

# References


P. Gargini, "ITRS Overview", http://www.itrs2.net/itrs-reports.html, July 2015

A. A. Istratov, C. Flink, H. Hieslmair, and E. R. Weber, Phys. Rev. Lett., 81, 1243 (1998).

J. D. McBrayer, R. M. Swanson, and T. W. Sigmon, J. Electrochem. Soc., 133, 1242 (1986).

Y. Shacham-Diamand, A. Dedhia, D. Hoffstetter, and W. G. Oldham, J. Electrochem. Soc., 140, 2427 (1993).

F. Lanckmans and K. Maex, Microelectron. Eng., 60, 125 (2002).

R. Hoofman, G. J. Verheijden, J. Michelon, et al., Microelectronic Engineering 80, 337-344 (2005)

J-Q Zhou, W Sun, H-Y Zhang, et al., ECS Transactions 34(1) 335-341 (2011)

M. Baklanov, J-F de Marneffe, D. Shamiryan, A. M. Urbanowicz, Hualiang Shi, T.V. Rakhimova, H. Huang, P.S. Ho, J. App. Physics 113, 041101 (2013)

K Holloway, P. Fryer, C. Cabral, JME Harper, P. J. Bailey, J. Appl. Phys 71(11) (1992) 5433 -44

L. Y. Yang, D. H. Zhang, C. Y. Li, P. D. Foo, Thin Solid Films 462-463 (2004) 176-181

B-S Nguyen, J-F Lin, D-C Perng, App. Phys. Letters 104 (2014) 082105

T.B. Massalski, "Binary Alloy Phase Diagrams", 2nd ed., pp 1467 (1990)

I. Goswami, R. Laxman, *Semiconductor International 27(5)* pp 49 (2004)

Li et al., Journ. Electrochem. Soc. 154(12) (2007) D642-D647

Fuchs, K.; Mott, N. F., Proc. of the Cambridge Philos. Soc., 34(01) (1938), p.100

Arunagiri, T. N.; Zhang, Y., et al., App. Phys. Lett. 86(8) (2005), pp 083104/1-3

Austin, D.Z., Jenkins, M.A, Allman, D, et al., Chemistry of Materials 29(3) (2017) 1107-1115

Mun, K-Y, Hong, T.E., Cheon, T.; et al., Thin Solid Films 562 (2014) pp 118-125

Lin, JH., Lee, JH., Hsu, CS. et al. Journal of Elec Materi 38: 2251 (2009)

N. Tsyntsaru, G. Kaziukaitis, C. Yang, H. Cesiulis, H. G. G. Philipsen, M. Lelis, J.-P. Celis, J Solid State Electrochem 18 (2014), 3057-3064

J. Shin, A. Waheed, W.A. Winkenwerder, H-W. Kim, K. Agapiou, R.A. Jones, G.S. Hwang, J.G. Ekerdt, Thin Solid Films 515 (2007) 5298-307

L.B. Henderson, J.G. Ekerdt, Thin Solid Films 517 (2009) 1645 - 1649.

D. Cristeaa, b, A. Crisanb, N.P. Barradasc, E. Alvesc, C. Mouraa, F. Vaza, L. Cunha, Applied Surface Science V. 285-A, pp 19-26 (2013)

K. Barmak, C. Cabral, K. P. Rodbell, J. M. E. Harper, J. Vac. Sci. Technol. B 24(6) (2006) 2485-98.

I. Goswami, R. Laxman, Semiconductor Internatl. 27 (2004) 49-54

H. Kim, C. Cabral, C. Lavoie, S.M. Rossnagel J. Vac. Sci. Technol. B 20(4) (2002) 1321-26.

K-Y Mun, T-E Hong, T Cheon, Y Jang, B-Y Lim, S Kim, S-H Kim, Thin Solid Films 562 (2014) 118-125

H. Kim, C. Cabral, C. Lavoie, S.M. Rossnagel J. Vac. Sci. Technol. B 20(4) (2002) 1321-26.

J. Shin, H.-W. Kim, G.S. Hwang, J.G. Ekerdt, Surf. Coat. Technol. 201 (2007) 9256-59.

Venables, J.A; Spiller, GDT; Hanbucken, M; Reports on Progress in Physics 47 (1984) pp 399

Nair, B; Priyadarshini, B.G.; AIMS Materials Science 3 (2016) pp 1022-1053

J.M. McGlonea, K.R. Olsenb, W.F. Sticklec, J.E. Abbottc, R.A. Pugliesec, G.S. Longc, D.A. Keszlerb, J.F. Wagera, Journal of Alloys and Compounds, V 650, pp 102-105 (2015)

J.-H. Shin, A. Waheed, W.A. Winkenwerder. H.-W. Kim, K. Agapiuo, R. A. Jones, G. S. Hwang, J. G. Ekerdt, *Thin Solid Films* 515 (2007) 5298

Hyun Woo Kim, "Structure and properties of amorphous metallic alloys: a first principles study", PhD dissertation, University of Texas Austin, OCLC 700073548 (2010)

D. Bost, H-W Kim, C-Y Chou, G.S. Hwang, J.G. Ekerdt, Thin Solid Films 662 (2017) pp 56 - 64

J. L. Pinney, Proc. R. Soc. A 319 (1970) 479.

J. L. Pinney, Nature 266 (1977) 309.

P. H. Gaskell, Amorphous Metals (eds H. Matyja and P. G. Zielinski), World Scientific Publishing, Singapore, 1985, pp. 35-57.

P. Lamparter, Phys. Scr. T57 (1995) 72-78.

W. K. Luo, H. W. Sheng, F. M. Alamgir, J. M. Bai, J. H. He, E. Ma, Phys. Rev. Lett. 92 (2004) 145502.

H. W. Sheng, W. K. Luo, F. M. Alamgir, J. M. Bai, E. Ma, Nature 439 (2006) 419.

D. Bost, J.G. Ekerdt; Thin Solid Films 558 (2014) pp 160 - 164

Chawla, N., Venkatesh, S.H., Singh, D.R.P. et al. J. of Materi Eng and Perform 22: 1085 (2013)

L. B. Henderson, J. G. Ekerdt, *Thin Solid Films* 517 (2009) 1645

Fadley, C.S.; J. Electron Spectroscopy and Related Phenomena 178 (2010) 2-32

NIST X-ray Photoelectron Spectroscopy Database, 4.1 (NIST, Gaithersburg, 2012)

NIST X-Ray Mass attenuation Coefficients Database, Table 3, http://physics.nist.gov/PhysRefData/XrayMassCoef/ElemTab/z44.html

C.D Wagner, et al. Surface Interface Anal. 3 (1981) 211

R. Kwok, XPSPEAK 4.1, http://www.uksaf.org/software.html

H. Okamoto, P-Ru, Binary Alloy Phase Diagrams 2$^{nd}$ ed. 3 (1990) 2978

L. B. Henderson, J. G. Ekerdt, Thin solid Films 517 (2009) 1645-1649

J.-H.Shin, H.-W.Kim, K.Agapiou, et al., J. Vac. Sci. Tech., A26 (2008) 974

J. Paschool, H. Kleykamp, F Thummler, J. Less Common Met. 98 (1984) 279

Li et al., Journ. Electrochem. Soc. 154(12) (2007) D642-D647

Fuchs, K.; Mott, N. F., Proc. of the Cambridge Philos. Soc., 34(01) (1938), p.100

G. Raghavan, C. Chiang, et al., TSF 262 (1995) 168-176

D. Bost, H-W Kim, C-Y Chou, G.S. Hwang, J.G. Ekerdt, Thin Solid Films 662 (2017) 56 - 64

J. Rodriguez, C. Truong, J. Corneille, D. Goodman, J. Phys Chem, 96 (1992) 334-341

H. Kim, S-H Lee, WT Lee, S Ganguli, H-C Ha, SH Yu, US Patent 20130146468 (2013) 2

Hyun Woo Kim, "Structure and properties of amorphous metallic alloys: a first principles study", PhD dissertation, University of Texas Austin, OCLC 700073548 (2010)

H. Li, D.B. Farmer, R.G. Gordon, Y. Lin, J. Vlassak, J. Electrochem. Soc. 154(12) (2007) D642-47.

K. Fuchs, N.F. Mott, Proc. Cambridge Philos. Soc., 34(01) (1938), 100-108.

G. Raghavan, C. Chiang, P.B. Anders, S-M Tzeng, R. Villasol, G. Bai, M. Bohr, D.B. Fraser, Thin Solid Films 262 (1995) 168-76.